TECHNICAL UNIVERSITY OF CRETE
SCHOOL OF ENVIRONMENTAL ENGINEERING

THESIS

Validation using eddy covariance data and SWEUS model for the calculation of the energy balance at the center of Heraklion city

PANAGIOTAKIS EMMANOUIL

COMMITTEE

Professor Dionisia Kolokotsa (Supervisor)

Professor Mihalis Lazaridis

Dr. Stavros Stagakis

Chania November 2020

Acknowledgement

In full gratitude, I would like to acknowledge the following individuals who encouraged, inspired, supported, assisted to help my pursuit of a master degree.

Primarily, I want to thank my advisor Professor Denia Kolokotsa for the encourage of my research, the advice, for discussions and all the support through this period which has been priceless.

Beside my supervisor, I would like to thank the rest of my thesis committee Prof. M. Lazaridis for being part of this thesis and Dr. S. Stagakis helping me with the data. Thank you both for your comments and help on the research.

Moreover, many thanks to FORTH and RSLab.gr for hosting me during this period, providing technical and scientific support as well as data necessary for this thesis. Especially my collaborators, Kostas Politakos and Dr. Zina Mitraka, at RSLab.gr for the sharing great ideas and helping me out with their knowledge get through difficulties.

Special Thanks to my Lab head at RSLab.gr, Dr. Nektarios Chrysoulakis helping me to deal with Remote Sensing and Urban Climate Research fields. Thank you for all your support and trust from the very first steps of my research career and throughout all these years.

Finally, special thanks to my family, who supported me the whole time. Thank you for all of the sacrifices that they have made on my behalf and make it possible for me to. Also, my friends that supported me and gave me the courage to continue. Thank you for hear me and help me with your support.

Abstract

The present thesis aims to study the estimation of urban energy balance using Surface Urban Energy and Water Scheme and the impact of Nature Based Solutions (NBS) on the urban environment. The Surface Urban Energy and Water balance Scheme (SUEWS) is used to quantify the impact of NBS in the city of Heraklion, Crete, Greece, a densely built urban area. Local meteorological data and data from an Eddy Covariance flux tower installed in the city center are used for the model simulation and evaluation. Five different scenarios are tested by replacing the city's roofs and pavements with green infrastructure, i.e. trees and grass, and water bodies. The NBS impact evaluation is based on the changes of air temperature 2m above the ground, relative humidity and energy fluxes. A decrease of the air temperature is revealed, with the highest reduction (2.3%) occurring when the pavements are replaced by grass for all scenarios. The reduction of the air temperature is followed by a decrease in turbulent sensible heat flux. For almost all cases, an increase of the relative humidity is noticed, accompanied by a considerable increase of the turbulent latent heat flux. Therefore, NBS in cities change the energy balance significantly and modify the urban environment for the citizens' benefit.

Contents

List of Figures

List of Tables

List of Abbreviations

Q^*	Net all-wave radiation
Q_F	Anthropogenic heat flux
Q_H	Turbulent Sensible heat flux
Q_E	Turbulent Latent heat flux
ΔQ_s	Net storage heat flux
P	Precipitation
I_e	Water supplied by irrigation or street cleaning
E	Evaporation
R	Runoff
ΔS	Net change in the water storage
$K_\downarrow$	Shortwave incoming radiation
$K_\uparrow$	Shortwave outgoing radiation
$L_\downarrow$	Longwave incoming radiation
$L_\uparrow$	Longwave outgoing radiation
F_{CLD}	Cloud fraction
ε_0	Emissivity of surface
ε_{clear}	Clear-sky emissivity
σ	Constant of Stefan-Boltzmann
T_0	Surface temperature
ρ_{pop}	Population density
$\alpha_{F0,1,2}$	Anthropogenic heat flux coefficients
$a_{1,2,3}$	OHM coefficients
f	Surface cover fraction
ρ	Density of air
c_ρ	Specific heat capacity of air at constant pressure
VPD	Vapor pressure deficit
r_{av}	aerodynamic resistance
r_s	Surface resistance
r_{av}	Rate at which water vapor is transported by turbulence between the surface and atmosphere
g_s	Surface conductance
S	slope of the saturation vapour pressure curve
γ	Psychrometric constant
LAI	Leaf area index

g	Control exerted function
G_1	Constant for g_s
T_{air}	Air temperature
p	pressure
RH	Relative humidity
U	Wind speed
z_0	Roughness length
z_h	Displacement height
$\Delta\theta$	Soil moisture deficit
Δq	Specific humidity deficit

1.
INTRODUCTION

1. Introduction

Due to the increase of the population in cities [1,2], the deep understanding of the driving forces that influence the urban environment is of major importance. The urbanization impacts the environment in several ways [3], as it affects the urban climate and makes cities potentially vulnerable. Studies about extreme weather conditions connect the city structure and characteristics with these conditions. Specifically, a natural hazard appears to be exacerbated by the urban form that contains factors as urban surface cover, urban fabric, and surface structure [4]. The type of surface cover in urban areas can increase the in-surface runoff and sensible heat emissions but also reduce the evaporation to the boundary layer of an urban environment in comparison to a naturally vegetated area. The implications of the changes in urban surface cover have an impact on human comfort, flooding, pollutant dispersion mixing of the boundary layer. Even though such fluxes are not measured, they are very important for the political management and decision-making of the competent authorities on a spatial scale, whether at the neighborhood, block, or city level[5].

According to various studies [6–9], resilience and sustainability should be taken into account in cities 'management in order to address the emerging challenges as well as the effects of climate on a large scale. The anthropogenic activity in urban areas changes considerably the water and energy use. Surface cover alterations in the urban environment increase the sensible heat emissions and surface runoff and reduce evaporation, compared to the natural environment [8]. This is mainly due to the materials used for the construction, lack of vegetation, and the emission of pollutants that affect the net all-wave radiation. The climate of an urban region is influenced directly by the modification of the energy fluxes into the atmosphere. Therefore, the study of the energy in the urban areas is essential. According to S. Rafael[6] there are three ways to approach and study the energy fluxes. Those are:

- exploit the turbulent flux measurements from the Eddy Covariance (EC) method.
- use a combined method with flux measurements and simulations.
- use models that are designed to model the energy balance in urban environment to link the surface energy balance with the climate.

With the third method, the surface cover can be modified to study the energy fluxes and climate behaviors among different scenarios of surface cover patterns inside a city.

The energy balance and consequently the energy fluxes are affected by several atmospheric variables. Net all-wave radiation fluxes are influenced by the solar radiation. Turbulent sensible and latent heat fluxes are influenced by atmospheric humidity, air temperature, and wind speed. Soil moisture affects the latent heat, defined by precipitation. In turn, energy fluxes also affect the atmospheric variables [10]. Modifying the surface fraction quota, different scenarios of energy fluxes can be studied for the improvement of sustainability in urban environments.

Sustainability is defined as the transformation of a residential area for the optimal support of the environmental and social conditions to human security, wellbeing and health [11].The sustainability of an urban environment can be supported using different alternatives such as Nature Based Solutions (NBS), or cool and highly reflective materials [12,13] in order to reduce the temperature and thermal comfort. There is a strong interest in solutions that are based on natural ecosystems and lead to renaturing cities [14]. Studies on ecosystem-based solutions seem to be useful for water management, air quality, public health, and well-being [15]. Moving from an ecosystem-based approach of NBS to adapt and limit climate change impacts could be the solution for improving human health and well-being [16].

NBS determines actions that are based on the copy, the inspiration or the support from nature [17]. According to Somarakis [18], NBS is the deployment of various features and processes that are inspired and supported by nature. This leads to the adoption of sustainability in urban, rural, and natural environments at various scales while dealing with social, economic, or environmental challenges providing several benefits that support sustainable development and resilience.

Similar studies have been performed with modeling tools to predict the climate in urban areas by increasing the greenery inside the urban area or using cool roofs materials and cool pavements

[19,20]. In Portugal, Rafael et al.[8] studied the possible scenarios of the future climate change using SUEWS and Weather Research and Forecasting Model (WRF). In their study, the simulation that used to calculate the incoming and outgoing radiation was based at the Representative Concentration Pathway Scenario [21] that using the greenhouse gas emissions and concentration that leads to the balance of incoming and outgoing radiation of the atmosphere due to the changes in the atmospheric composition. For the simulation of the forcing meteorological data, present and future, the WRF and MPI-ESM (Max Planck Institute for Meteorology Earth System Model[22]) models were used. To simulate both of the scenarios, the parameters of the population density, land cover fractions and related parameters were stable. Rafael et al. [6] use SUEWS for the city of Porto to study the behavior of energy balance inside the city according these two scenarios.

Another study in Einthoven uses NBS to assess the impact in local changes of heat fluxes and urban compaction[23]. Also, the Surface Urban Energy and Water Balance Scheme model has been tested and evaluated in different cities like Porto [8,24], Vancouver and Los Angeles [5,25], London and Swidon [3], Helsinki and Montreal[26], Dublin[27,28], Shanghai[29]. The work performed in the framework of the BRIDGE project focuses on the urban metabolism using different models for the estimation of the local scale energy, water, carbon and pollutant fluxes [9]. Similar scenarios are studied by Li et al [12] to study the urban heat island over the Baltimore-Washington metropolitan area using Princeton Urban Canopy Model. Both of them use Weather Research and Forecasting model to supply the forcing meteorological data. The results seem to be similar even though the methods differ. In addition, Manoli et al [30] pinpoint that using low vegetation to reduce the temperature through evapotranspiration could work mainly in cities with dry climatic conditions but not in tropical cities with high precipitation (P >1000mm yr^{-1}). In tropical cities would be more useful to increase of shading and ventilation than using evaporative cooling. Also, the high albedo materials although they result in the reduction of the surface temperatures of cities they have a heating penalty during winter period [31,32].

To this end, the aim of the present study is to evaluate different NBS scenarios for the city of Heraklion, Crete Greece. The Surface Urban Energy and Water Balance Scheme (SUEWS) model is used to investigate the energy fluxes in the center of the city [5,33–36]. The surface cover of the city is changed to evaluate the energy fluxes when NBS are integrated in the city context.

The Study is structured in three sections. Section 2 includes the methodology, the study area and the data, as well as a description of the SUEWS model and its evaluation in the study area and the various NBS scenarios for the city of Heraklion are analyzed and discussed. Section 3 summarizes and presents the conclusions of the overall work.

2.

MATERIALS AND METHODS

2. Materials and Methods

The methodology followed in the present work is depicted in Figure 2.1. The city of Heraklion, Crete, Greece is selected as a case study for the following reasons:

- Detailed meteorological data from a meteorological station installed in the center of the city.
- Access to EC tower and energy fluxes data.

The SUEWS model (described in Chapter 2.1) is utilized to simulate the various fluxes in the city of Heraklion in Greece. The SUEWS model of Heraklion is evaluated versus real data extracted by the EC tower. Data set from July 2018 is used for the evaluation of the model under the specific urban conditions. To evaluate the model, meteorological and net all-wave radiation data are collected from the EC tower and the radiometer respectively. The monitoring procedure and mechanisms are described in Chapter 3.

The evaluated model is then used for the modeling of the incorporation of NBS in the urban area and improvement of the local environment.

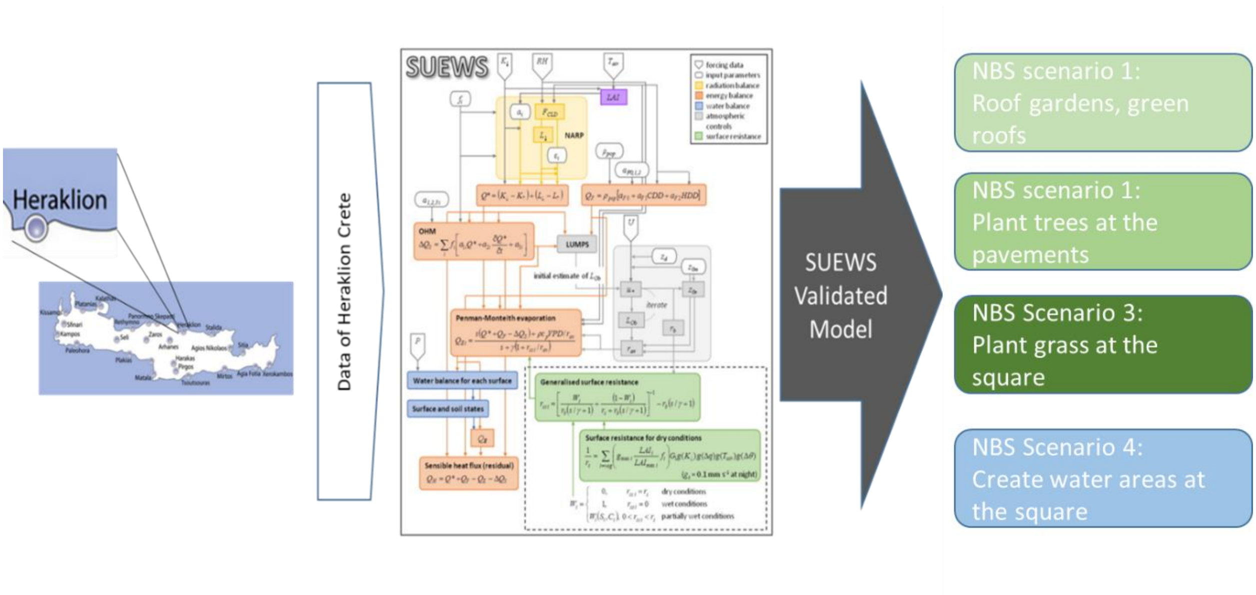

Figure 2.1 The workflow for the NBS evaluation in Heraklion, Crete, Greece.

2.1 Description of the model

The SUEWS model is a simple simulation model of energy and water fluxes. The model simulates energy balance [37],

$Q^{*} + Q_F = Q_H + Q_E + \Delta Q_S$ (Eq. 1)

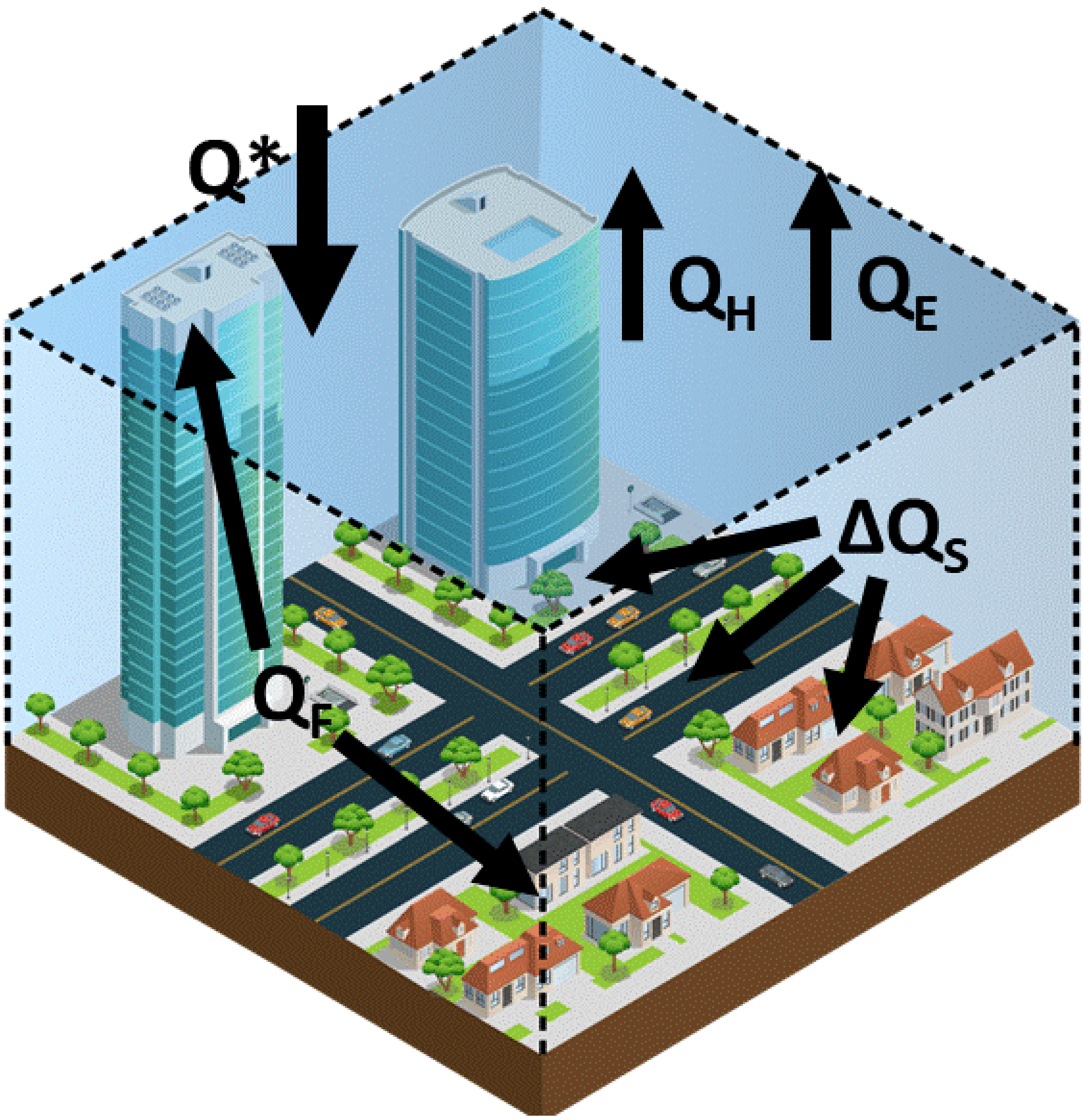

Figure 2.2. The energy fluxes of SUEWS model

where Q^* is the net all-wave radiation, Q_F is the anthropogenic heat flux, Q_H is the turbulent sensible heat flux, Q_E is the turbulent latent heat flux and ΔQ_s is the net change in heat storage.

Water balance in urban areas is expressed by [38],

$P + I_e = E + R + \Delta S$ (Eq. 2)

where P is precipitation, I_e is the water supplied by irrigation or street cleaning, E is the evaporation, R is the runoff (including above-ground runoff and deep soil runoff) and ΔS is the net change in the water storage (including water in the soil and water held on the surface).

The specialization of SUEWS is mainly for urban areas and examines seven types of surface. The first type is the paved surfaces areas, i.e. roads, pavements and car parks, the second type is buildings, the third is evergreen trees including shrubs, the fourth is deciduous trees including shrubs, the fifth is grass, the sixth is bare soil and the seventh is open water like swimming pools, rivers etc.

SUEWS development at first was focused on urban water balance model [38] and the urban evaporation-interception scheme [39]. The SUEWS model is further developed with the addition of the following sub-models:

- The Objective Hysteresis Model (OHM) that calculates the ΔQ_S from Grimmond[40].
- The Net All-wave Radiation Parameterization (NARP) [41] that provides the Q*.
- The Local-scale Urban Meteorological Parameterization Scheme (LUMPS) [42] that calculates an initial estimate of the atmosphere' s stability.

The benefits of SUEWS are mainly two, i.e. the simplicity of the model and the undemanding requirements for inputs compared to other models. As a result, the execution for different years and multiple grids can be accomplished using typical computing facilities [3]. SUEWS can be characterized either as an urban-scale model for standalone use or as a tool for decision-making by customizing scenarios for the urban planners and policy makers that fit their needs [43].

SUEWS was initially developed, parameterized, and evaluated using data that were collected from Vancouver suburban areas [5,38,39]. Other evaluations have been performed using data from cities such as Los Angeles [5], Montreal and Helsinki [33,44] and Dublin[45].

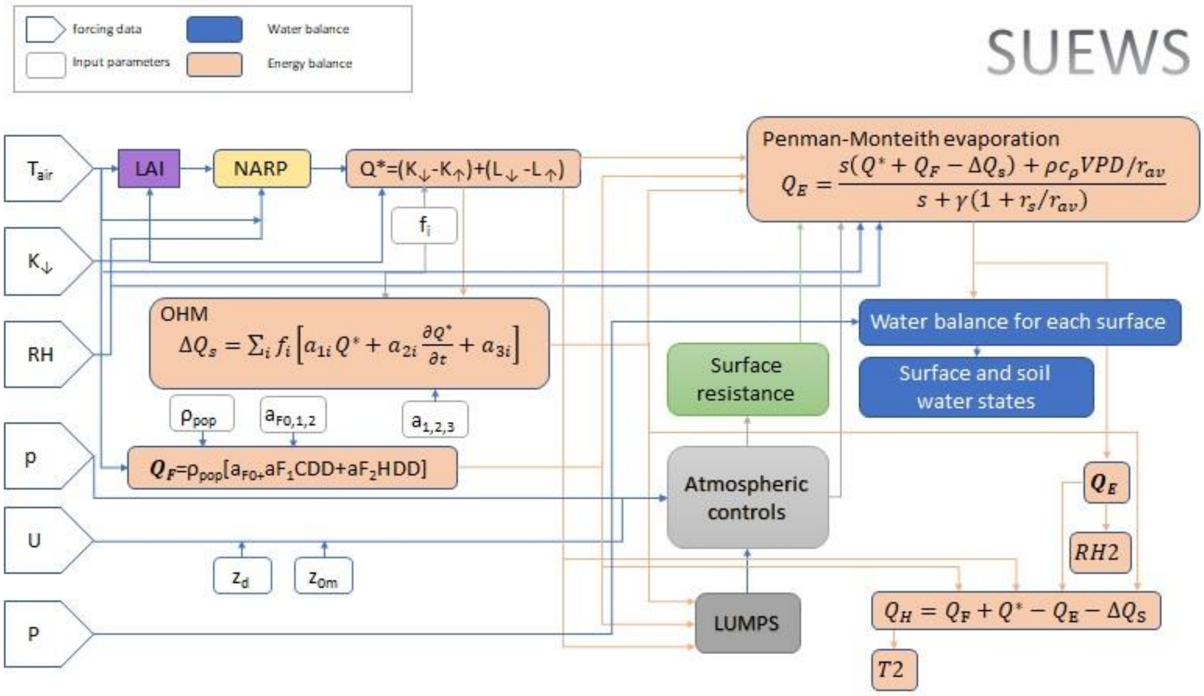

Figure 2.3 Overview of SUEWS model processes.

2.2 Net all-wave radiation model

Net all-wave radiation is modeled using all radiation components,

$$Q^* = (K_\downarrow - K_\uparrow) + (L_\downarrow - L_\uparrow) \quad \text{(Eq.3)}$$

where $K_\downarrow$ is the shortwave incoming radiation, the $K_\uparrow$ is the outgoing shortwave radiation, $L_\downarrow$ is the longwave incoming radiation and $L_\uparrow$ is the longwave outgoing radiation. Shortwave incoming radiation is included to the input data while shortwave outgoing, longwave incoming and outgoing radiations are extracted using incoming shortwave radiation.

The calculation of outgoing shortwave radiation($K_\uparrow$) is performed using a bulk albedo(a). Bulk albedo is modeled using the albedo of the different type of surfaces with the fractions of the area scheme. The values of the albedo used in SEUWS (Table 2-1) are selected from Oke (1987) and the modeled bulk albedo in Heraklion is 0.14, that was calculated using the average albedo for all the fractions, also used for London and Swindon[3] Vancouver and Los Angeles[5]. The specific values are not appropriate for the Heraklion site due to the lack of observational data. The methodology proposed by Ward[3] is adopted in the present case to perform adjustments that lower the SEUWS bulk albedo due to the presence of buildings and paved surfaces. Moreover, the specific methodology enables the bulk albedo changes due to seasonal and vegetation variations (e.g. deciduous trees).

Table 2-1. The original values for albedo and emissivity have been used from Ward 2016. Different albedo values have been used for leaf-off/leaf-on(Min/Max) for deciduous trees		
Surface type	Original Albedo	Emissivity
Paved	0.12	0.95
Buildings	0.15	0.91
Evergreen trees	0.10	0.98
Deciduous trees	0.15-0.18	0.98
Grass	0.21	0.93
Bare soil	0.21	0.94
Water	0.10	0.95
Heraklion study site	0.14	-

The calculation of incoming longwave radiation ($L_{\downarrow}$) is performed using the cloud cover. Cloud cover is estimated using T_{air} and RH[41,46]. There is an overestimation in the calculation of incoming longwave radiation[47] that is due to the empirical relation that is used for the determination of cloud fraction[46]. :

$$F_{CLD}\,(RH, T_{air}) = 0.185[\exp\{(0.00019\,T_{air}+0.015)RH\}-1 \qquad \text{(Eq.4)}$$

The $L_{\downarrow}$ is calculated using Eq. 5 [47],

$$L_{\downarrow}= [\varepsilon_{clear} +(1-\varepsilon_{clear})\,F_{CLD}]\,\sigma T^4_{air} \qquad \text{(Eq.5)}$$

where ε_{clear} is the clear-sky emissivity and σ is the constant of Stefan-Boltzmann.

The calculation of outgoing longwave radiation ($L_{\uparrow}$) is performed using the effective radiative surface temperature T_0 and a small part from $L_{\downarrow}$[3],

$$L_{\uparrow}= \varepsilon_0 \sigma T^4_0 + (1 - \varepsilon_0)\, L_{\downarrow} \qquad \text{(Eq.6)}$$

Due to the inability of T_0 determination in large areas Offerle [41] use an approximation replacing T_0 with T_{air},

$$L_{\uparrow}= \varepsilon_0 \sigma T^4_{air} + 0.08K_{\downarrow}\,(1 - \alpha_0) + (1- \varepsilon_0)L_{\downarrow} \qquad \text{(Eq.7)}$$

where α_0 is the bulk surface albedo. Albedo and emissivity values can be found in Table 2-1.

2.3 Anthropogenic heat flux

Anthropogenic heat flux, Q_F, is the energy released as a result of human activities, including the energy released from buildings due to the use of electrical devices (for heating, cooling, etc.), the transportation and the human metabolism[48,49]. Q_F has a significant impact on the energy demand in an urban environment[50–53]. The Q_F is estimated from SUEWS on a daily basis according to Sailor and Vasireddy [54]:

$$Q_F = \rho_{pop}\,[\alpha_{F0} + \alpha_{F1}CDD + \alpha_{F3}HDD] \quad \text{(Eq.8)}$$

where ρ_{pop} is the population density. The coefficients $\alpha_{F0,1,2}$ can be specified separately for weekdays and weekends. Including the heating degree days(HDD) and cooling degree days (CDD) dependence in the formula Q_F is modeled with temperature variations reflecting the demand changes for building heating or cooling. The inventory data are used for the estimation of Q_F [55].

2.4 Net Change in Heat Storage

The calculation of net change in heat storage, ΔQ_S, is realized with Objective Hysteresis Model (OHM) [40]:

$$\Delta Q_s = \sum_i f_i \left[a_{1i} Q^* + a_{2i} \frac{\partial Q^*}{\partial t} + a_{3i} \right] \quad \text{(Eq.9)}$$

where f is the surface cover fraction for each surface type, i, and t is the time. The OHM coefficients $a_{1,2,3}$ are different for each surface type and are selected from the literature. The coefficients collected with different ways, most of the calculated from empirical fits to observational data [56–58] and the others form simulation studies [59–61].

The OHM seems to perform well at suburban sites during the summer months, according to the diurnal cycle shape, with a small underestimation during daytime. In the winter, there is an underestimation of ΔQ_S, so the coefficients have to be adjusted for two seasons [3]. The inability of this study to evaluate ΔQ_s is due to the lack of observational data.

Considering the three-dimensional structure of the urban surface and by including the wall area have been found that instead of improving performance using OHM there is a decrease when the walls are actually important at the site[62]. Even so, the expectation of building construction dependence seems to be reasonable. Arnfield and Grimmond [59] created a numerical model to nominate the dependence of $\alpha_{1,3}$ coefficients with the increase of height-to-width ration and materials density in buildings. The importance of considering the characteristics of buildings for the selection of appropriate coefficients values to set OHM is clear. Several values have been tested to connect with the environment and the urban structure [44,56,63].

2.5 Latent heat flux

The aerodynamic and surface resistances are required to model the turbulent latent heat flux, Q_E , using the Penman-Monteith equation (Penman, 1948; Monteith, 1965) modified for urban areas (Grimmond and Oke, 1991).:

$$Q_E = \frac{s(Q^* + Q_F - \Delta Q_S) + \rho c_\rho VPD/r_{av}}{s + \gamma(1 + r_s/r_{av})} \qquad \text{(Eq.10)}$$

where ρ is the density of air, c_ρ the specific heat capacity of air at constant pressure, VPD the vapor pressure deficit, s the slope of the saturation vapor pressure curve, γ the psychometric constant, r_{av} the aerodynamic resistance for water vapor and r_s the surface resistance. r_{av} determines the rate at which water vapor is transported by turbulence between the surface and atmosphere. The surface resistance is analogous to the canopy resistance in natural environments and describes the environmental controls on evaporation for the whole urban surface[5,40]. Its reciprocal is the surface conductance g_s. Despite several major land-surface models using g_s to calculate evaporation and photosynthesis[64–66], it is difficult to simulate g_s in a generalized way. Various approaches have been suggested and in SUEWS a Jarvis-Stewart formulation [5,67]is used:

$$g_s = \sum_i \left(g_{\max i} \frac{LAI_i}{LAI_{\max i}} f_i \right) G_1 g(K_\downarrow) g(\Delta q) g(T_{air}) g(\Delta\theta) \qquad \text{(Eq.11)}$$

where the sum is over the three vegetated surfaces and weighted by the surface cover fraction f of each surface i.

$g_{\max i}$is the maximum conductance for surface i, $LAI_{\max i}$ is the (maximum) leaf area index for each surface i and G_1 is a constant.

The functions $g(K_\downarrow)$, $g(\Delta q), g(T_{air}), g(\Delta\theta)$ describe the control functions exerted by the incoming shortwave radiation, specific humidity deficit, air temperature and soil moisture deficit, respectively. In SUEWS_v2016a, the soil moisture deficit beneath vegetated surfaces is used, where soil moisture deficit is the loss of moisture from soil that hasn't been replaced from precipitation. However, various empirical relations and alternative methodologies are provided in the literature for these control functions [5,67,68].

A new functional dependence on the control functions is presented by Ward[3] with the main objective of relaxing the control of soil moisture on evaporation. With the new set of parameters, the limiting $\Delta\theta$ is much larger and thus more suitable for the Heraklion site. The new relations are designed to be less restrictive so that unrealistic values of the surface conductance (and Q_E) are avoided. At suburban areas the diurnal pattern of both observed and modelled g functions exhibit the expected behavior during summer, mainly determined by the changing ratio of VPD/Q_E where VPD is the vapor pressure deficit. Conductances are much smaller and have a less clearly defined pattern in areas with less vegetation, reduced moisture availability and lower evaporation rates. In winter the diurnal cycle is shorter, more symmetrical and smaller in amplitude at suburban area, whilst observed night-time values are higher at both urban and suburban sites, probably due to higher wind speeds and damp surfaces. Observed g functions are also higher than suggested by the model during winter daytimes[3].

2.6 Sensible Heat Flux

The turbulent sensible Heat flux is calculated as the residual of energy balance:

$$Q_H = Q^* + Q_F - \Delta Q_S - Q_E \qquad \text{(Eq.12)}$$

3.

DESCRIPTION OF THE SITE AND DATA REQUIREMENTS FOR SUEWS

3. Description of the site and data requirements for SUEWS

3.1 The city of Heraklion

The study focuses on the city of Heraklion (35° 20′ N, 25° 8′ E). The city of Heraklion is the largest city in the island of Crete and one of the larger in Greece. Heraklion has been selected in the past as test urban area for the measurement of turbulent fluxes using a specific EC tower installed in the framework of URBANFLUXES project [69] which is part of the International Association for Urban Climate Urban Flux Network [70]. Heraklion is selected due to its cover/morphology, climate and traffic/commuter patterns. The types and properties of buildings are highly variable across the city. Residential neighborhoods and commercial areas are included inside the city center, a mix of low and mid-rise buildings. Most of the buildings in the residential area of the city center are mainly old without any thermal insulation or building services such as heating ventilation and air conditioning. In the center of the city the density of buildings is quite high (40-70%) while it is lower in the suburbs (10-30%). The EC tower has been installed in the core of the Heraklion city center (35° 20′ 10″ N, 25° 7′ 58″ E, terrain elevation 30m above sea level [71]. The position of the EC tower is marked with a yellow cross in Figure 3.1.

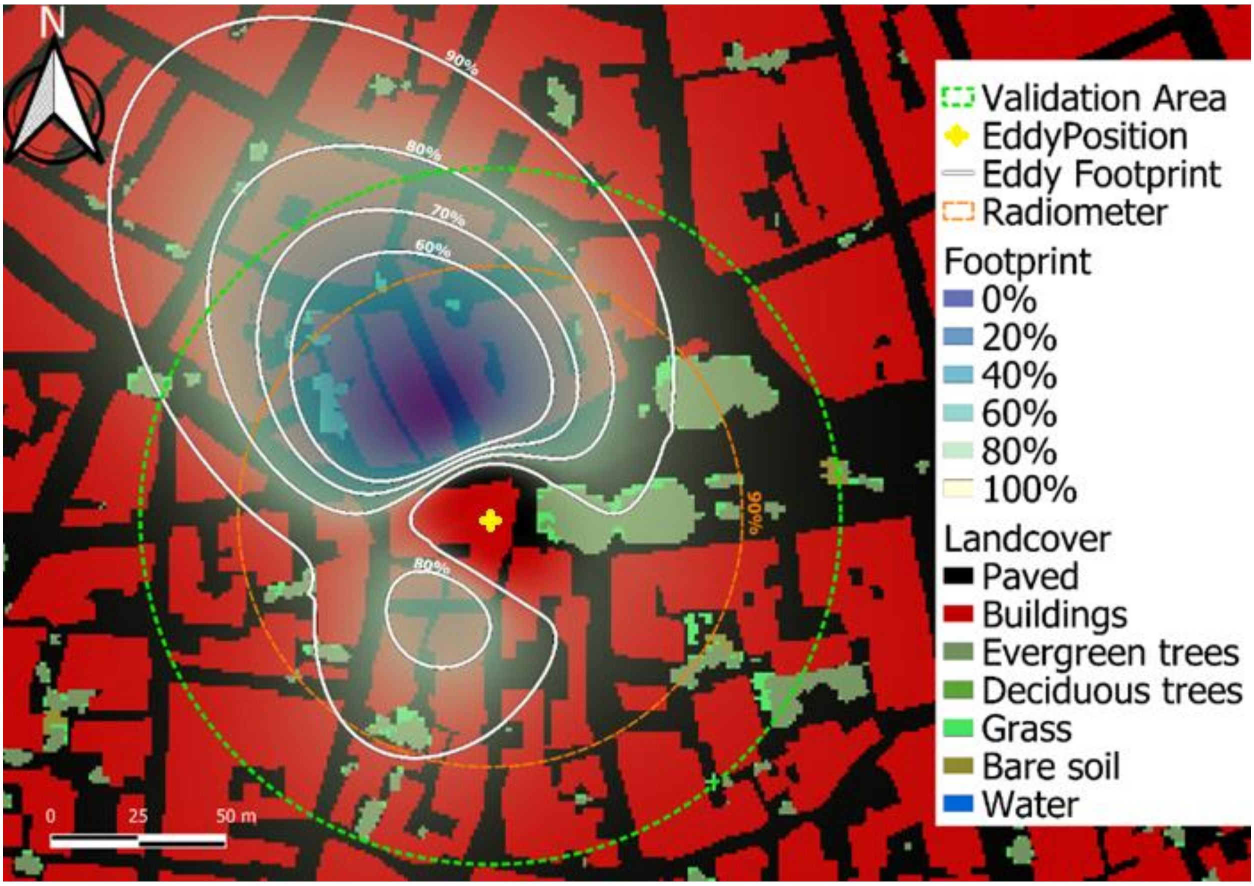

Figure 3.1 This image shows site of evaluation area. The EC tower and the simulated footprint that shows the source area with the rate influence. The source area of the radiometer with the rate influence.

3.2 Monitoring data requirements

The required data for the present study are:

- Meteorological and radiation data from the sensors installed on the EC tower (hourly averaged data).
    - incoming shortwave radiation ($K_{\downarrow}$)
    - air temperature (T_{air})
    - air pressure (p)
    - relative humidity (RH)
    - wind speed (U)
    - precipitation (P)
- Population density data from the national statistical services.
- Surface cover data. In this study, Surface Cover data and Digital Surface Model (DEM) for buildings and trees are extracted from remote sensing [69,72]. Roughness length and displacement height are extracted from DEMs for trees and buildings using the

Morphometric Calculator tool from UMEP processing tools, that extracts Morphometric parameters from a DSM based on a specific point in space[43,73]. Due to the lack of initial soil moisture data the value is set equal to 100% according to developers[74]. The characteristics of the site are tabulated in Table 3-1.

Remote sensing is a tool that has been developed the last years to support landscape ecological research to pattern recognition, state analysis and landscape trajectories, as well as landscape properties recognition. Combined with Geographical Information Systems (GIS), biophysical first principles and modern spatial analysis methods, powerful retrievals and interpretations can be achieved of spatial and temporal scales. The primary principles of remote sensing are the two following: a) the image collection of the earth surface and the atmosphere from a long-distance using satellites or aircrafts, and b) the record of electromagnetic radiation that coming from Earth surfaces and objects. This can be achieved using a source that is projected to the earth surface to record the emissions or by recording the reflected light from the ground. Detecting and recording reflected radiation is important because objects on the ground reflect and absorb radiation differently depending on the surface, and thus they reflect the incoming energy at different intensities along a range of wavelengths[75]. In this study Land Cover data and Digital Elevation Model (DEM) for buildings and trees are extracted from remote sensing. Roughness length and displacement height are extracted from DEMs for trees and buildings using the Morphometric Calculator. Due to the lack of initial soil moisture data the value is set equal to 100% [74].

Table 3-1. Characteristics of the source area for the Heraklion site.	
Surface cover fractions	
• Paved	0.404
• Buildings	0.532
• Evergreen trees	0.052
• Deciduous trees	0.000
• Grass	0.011
• Bare soil	0.001
• Water	0.000
Population density [ha-1]	57
Mean building/tree height [m]	12/8.2
Roughness length [m] (z_0)	1.9
Displacement height [m] (z_d)	14.2
Measurement height [m]	27
Location	35° 20’ N, 25° 8’ E

3.3 Data collection equipment

The data used for analysis have been collected using an EDDY covariance system open path (Campel scientific Irgason). Irgason consist of an optical gas analyzer (CO_2, H_20) and a 3D sonic anemometer. Auxiliary sensors used are barometric air pressure, air temperature and net radiometer Kipp & Zonen CNR1. Irgason is at 27-meter height from the ground and CNR1 is at 24 meters.

It acquires point measurements of H_2O and CO_2 molar densities between the open path receiver and transmitter of the optical gas analyzer and 6 ultra-sonic transducers forming 3 pairs of 3D sonic anemometer. The wind speed is calculated using all three components of wind from the anemometer. The advantages are the colocation and synchronicity of the wind and the gas measurements that makes the corrections of the sensor separation unnecessary and the wind distortion is minimized. Also, there is installed, at the top of the tower, a thermistor temperature sensor that measures the ambient air temperature (T_{air}).

3.4 Eddy covariance method

As turbulent flux is considered the superposition of different sizes of eddies. According to Eddy Covariance theory, vertical turbulent flux of any scalar s can be mathematically deduced from the covariance of vertically rotated wind speed (w) and the mixing ratio of this scalar. Following the Reynolds decomposition, each variable in a turbulent motion can be described as the sum of a mean and a fluctuating part. According to the above, the general equation of the flux calculation can be given as:

$$F = \overline{\rho_d \cdot w \cdot s} = \overline{\rho_d} \cdot \overline{w's'} \qquad \text{(Eq.13)}$$

The mean components are indicated using over-bars and the fluctuating components using the primes. The time average of the fluctuating components (w’ and c’) are zero.

Several requirements should be satisfied to apply the method of eddy covariance. One of the common assumptions is that the mean vertical wind speed is zero. This assumption is valid enough selecting the measuring point around a flat area although the wind speed is not zero but the deviation is close to zero. The method of eddy covariance can be applied also in a sloping terrain, because it allows mathematically to force the vertical wind speed to zero by coordinate rotations, that is by rotating the mean wind vector to local streamlines. Also, the time series during the measurement period should be stationary (not dependent on time), even though the method of eddy covariance can be applied to lightly non-stationary conditions. Moreover, the source area of the flux measurements should be horizontally homogeneous to be representative the surface flux around the measurement site. The EC method demand rapid measurements of both wind speed and concentration. The ideal response frequency that should have the sensors and analyzers is at least 10Hz. Also, the resolution of the wind speed measurements should be at least ±0.05 $m*s^{-1}$ and for the temperature at 0.05 C^o, the concentration signal-to-noise ratio should be at least 30. The height of the tower also is critical, to reach the layer above the canopy the tower must be supported form a thin mast or rod that raises the sensor over three lateral dimensions at least. The measurements that derived from the equipment are shown in the Table 3-2

Table 3-2. The table with the output measurements and estimated values of the EC tower		
Label	Units, Format, or Range	Description
filename	-	Name of the raw file (or the first of a set) from which the dataset for the current averaging interval was extracted
date	yyyy-mm-dd	Date of the end of the averaging period
time	HH:MM	Time of the end of the averaging period
file_records	#	Number of valid records found in the raw file (or set of raw files)
used_records	#	Number of valid records used for current the averaging period
Tau	kg m-1 s-2	Corrected momentum flux
qc_Tau	#	Quality flag for momentum flux
rand_err_Tau	kg m-1 s-2	Random error for momentum flux, if selected
H	W m-2	Corrected sensible heat flux
qc_H	#	Quality flag for sensible heat flux
rand_err_H	W m-2	Random error for momentum flux, if selected
LE	W m-2	Corrected latent heat flux
qc_LE	#	Quality flag latent heat flux
rand_err_LE	W m-2	Random error for latent heat flux, if selected
gas_flux	µmol m-2 s-1(†)	Corrected gas flux
qc_gas_flux	#	Quality flag for gas flux
rand_err_gas_flux	µmol s-1 m-2(†)	Random error for gas flux, if selected
H_strg	W m-2	Estimate of storage sensible heat flux
LE_strg	W m-2	Estimate of storage latent heat flux

Table 3-2. The table with the output measurements and estimated values of the EC tower		
Label	Units, Format, or Range	Description
gas_strg	μmol s-1 m-2(†)	Estimate of storage gas flux
gas_v-adv	μmol s-1 m-2(†)	Estimate of vertical advection flux
gas_molar_density	mmol m-3	Measured or estimated molar density of gas
gas_mole_fraction	μmol mol-1(†)	Measured or estimated mole fraction of gas
gas_mixing_ratio	μmol mol-1(†)	Measured or estimated mixing ratio of gas
gas_time_lag	s	Time lag used to synchronize gas time series
gas_def_timelag	T/F	Flag: whether the reported time lag is the default (T) or calculated (F)
sonic_temperature	K	Mean temperature of ambient air as measured by the anemometer
air_temperature	K	Mean temperature of ambient air, either calculated from high frequency air temperature readings, or estimated from sonic temperature
air_pressure	Pa	Mean pressure of ambient air, either calculated from high frequency air pressure readings, or estimated based on site altitude (barometric pressure)
air_density	kg m-3	Density of ambient air
air_heat_capactiy	J K-1 kg-1	Specific heat at constant pressure of ambient air
air_molar_volume	m3 mol-1	Molar volume of ambient air
ET	mm hour-1	Evapotranspiration flux
water_vapor_density	kg m-3	Ambient mass density of water vapor
e	Pa	Ambient water vapor partial pressure
es	Pa	Ambient water vapor partial pressure at saturation

Table 3-2. The table with the output measurements and estimated values of the EC tower

Label	Units, Format, or Range	Description
specific_humidity	kg kg-1	Ambient specific humidity on a mass basis
RH	%	Ambient relative humidity
VPD	Pa	Ambient water vapor pressure deficit
Tdew	K	Ambient dew point temperature
u_unrot	m s-1	Wind component along the u anemometer axis
v_unrot	m s-1	Wind component along the v anemometer axis
w_unrot	m s-1	Wind component along the w anemometer axis
u_rot	m s-1	Rotated u wind component (mean wind speed)
v_rot	m s-1	Rotated v wind component (should be zero)
w_rot	m s-1	Rotated w wind component (should be zero)
wind_speed	m s-1	Mean wind speed
max_wind_speed	m s-1	Maximum instantaneous wind speed
wind_dir	° (degrees)	Direction from which the wind blows, with respect to Geographic or Magnetic north
yaw	° (degrees)	First rotation angle
pitch	° (degrees)	Second rotation angle
u*	m s-1	Friction velocity
TKE	m2 s-2	Turbulent kinetic energy
L	M	Monin-Obukhov length
(z-d)/L	#	Monin-Obukhov stability parameter
bowen_ratio	#	Sensible heat flux to latent heat flux ratio

Table 3-2. The table with the output measurements and estimated values of the EC tower		
Label	Units, Format, or Range	Description
T*	K	Scaling temperature
(footprint) model	-	Model for footprint estimation
x_offset	m	Along-wind distance providing <1% contribution to turbulent fluxes
x_peak	m	Along-wind distance providing the highest (peak) contribution to turbulent fluxes
x_10%	m	Along-wind distance providing 10% (cumulative) contribution to turbulent fluxes
x_30%	m	Along-wind distance providing 30% (cumulative) contribution to turbulent fluxes
x_50%	m	Along-wind distance providing 50% (cumulative) contribution to turbulent fluxes
x_70%	m	Along-wind distance providing 70% (cumulative) contribution to turbulent fluxes
x_90%	m	Along-wind distance providing 90% (cumulative) contribution to turbulent fluxes
un_Tau	kg m-1 s-2	Uncorrected momentum flux
Tau_scf	#	Spectral correction factor for momentum flux
un_H	W m-2	Uncorrected sensible heat flux
H_scf	#	Spectral correction factor for sensible heat flux
un_LE	W m-2	Uncorrected latent heat flux
LE_scf	#	Spectral correction factor for latent heat flux
un_gas_flux	µmol s-1 m-2(†)	Uncorrected gas flux
gas_scf	#	Spectral correction factor for gas flux

Table 3-2. The table with the output measurements and estimated values of the EC tower

Label	Units, Format, or Range	Description
spikes	8u/v/w/ts/co2 /h2o/ch4/none	Hard flags for individual variables for spike test
amp_res	8u/v/w/ts/co2 /h2o/ch4/none	Hard flags for individual variables for amplitude resolution
drop_out	8u/v/w/ts/co2 /h2o/ch4/none	Hard flags for individual variables for drop-out test
abs_lim	8u/v/w/ts/co2 /h2o/ch4/none	Hard flags for individual variables for absolute limits
skw_kur	8u/v/w/ts/co2 /h2o/ch4/none	Hard flags for individual variables for skewness and kurtosis
skw_kur	8u/v/w/ts/co2 /h2o/ch4/none	Soft flags for individual variables for skewness and kurtosis test
discontinuities	8u/v/w/ts/co2 /h2o/ch4/none	Hard flags for individual variables for discontinuities test
discontinuities	8u/v/w/ts/co2 /h2o/ch4/none	Soft flags for individual variables for discontinuities test
time_lag	8u/v/w/ts/co2 /h2o/ch4/none	Hard flags for gas concentration for time lag test
time_lag	8u/v/w/ts/co2 /h2o/ch4/none	Soft flags for gas concentration for time lag test
attack_angle	0, 1, 9	Hard flag for attack angle test
non_steady_wind	0, 1, 9	Hard flag for non-steady horizontal test
var_spikes	#	Number of spikes detected and eliminated for variable var
AGC	#	Mean value of AGC for LI-7500RS or LI-7200RS
RSSI	#	Mean value of RSSI for LI-7700, if present

Table 3-2. The table with the output measurements and estimated values of the EC tower		
Label	Units, Format, or Range	Description
var_var	-(‡)	Variance of variable var
w/var_cov	-(‡)	Covariance between w and variable var
extravar_mean	(‡)	Mean value of extravar

3.5 Preparation data

To run the model of SUEWS first the data must be prepared to the form needed for the plugin. There are 3 stages to run the model and there is also a post-processing to export graphs of the outputs (Figure 3.2). All the tools are part of the Urban Multi-scale Environmental Predictor (UMEP), an open source climate service tool presented as a plugin for QGIS.

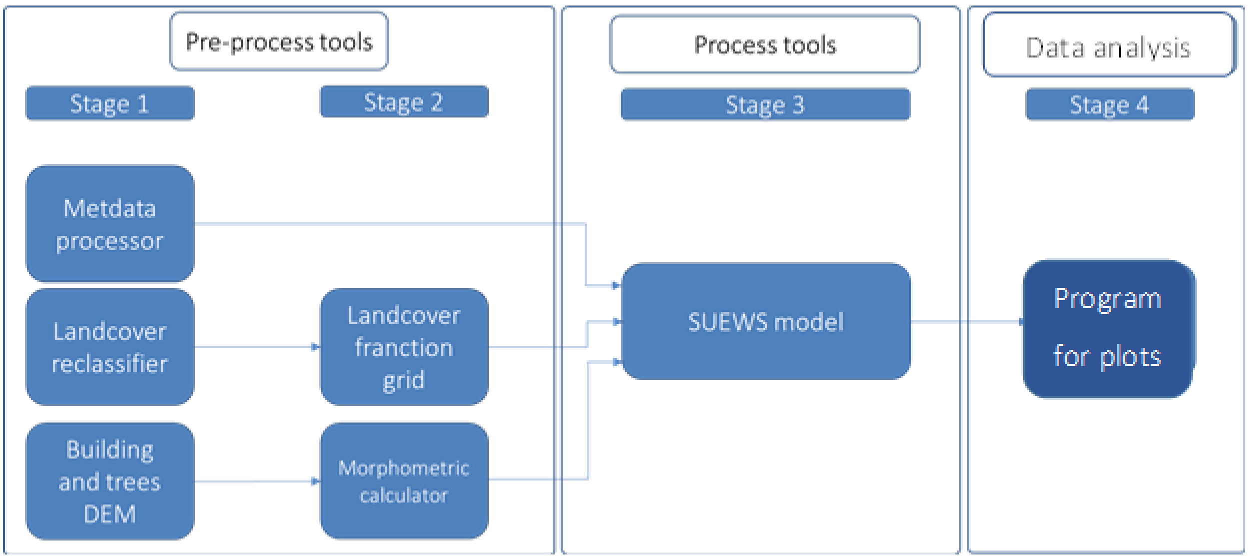

Figure 3.2 The stages that needed to run the model of SUEWS.

First the meteorological data have to be in a text file so can be converted in the preferred form using the Metdata processor. Metdata processor plugin (Figure 3.3) converts the data to another text file that is used as input to the model. In simple mode, the basic data needed to run so as it is seen in the figure only data with "*" are used. The output file from used as input to the model. As it is shown in the figure, every box is filled by the heading of each column inside the original text file. The time and meteorological variables have to match and then exported to the new text file.

The second part of first stage is to convert land cover into a new one with the 7 classes that are used to run the model. For the conversion there is another tool by UMEP is needed that is called Landcover reclassifier. The Land Cover Reclassifier (Figure 3.4) converts each fraction or a range of similar fractions of a landcover to one of the basic fractions that SUEWS use as input. The fractions that must be translated are:

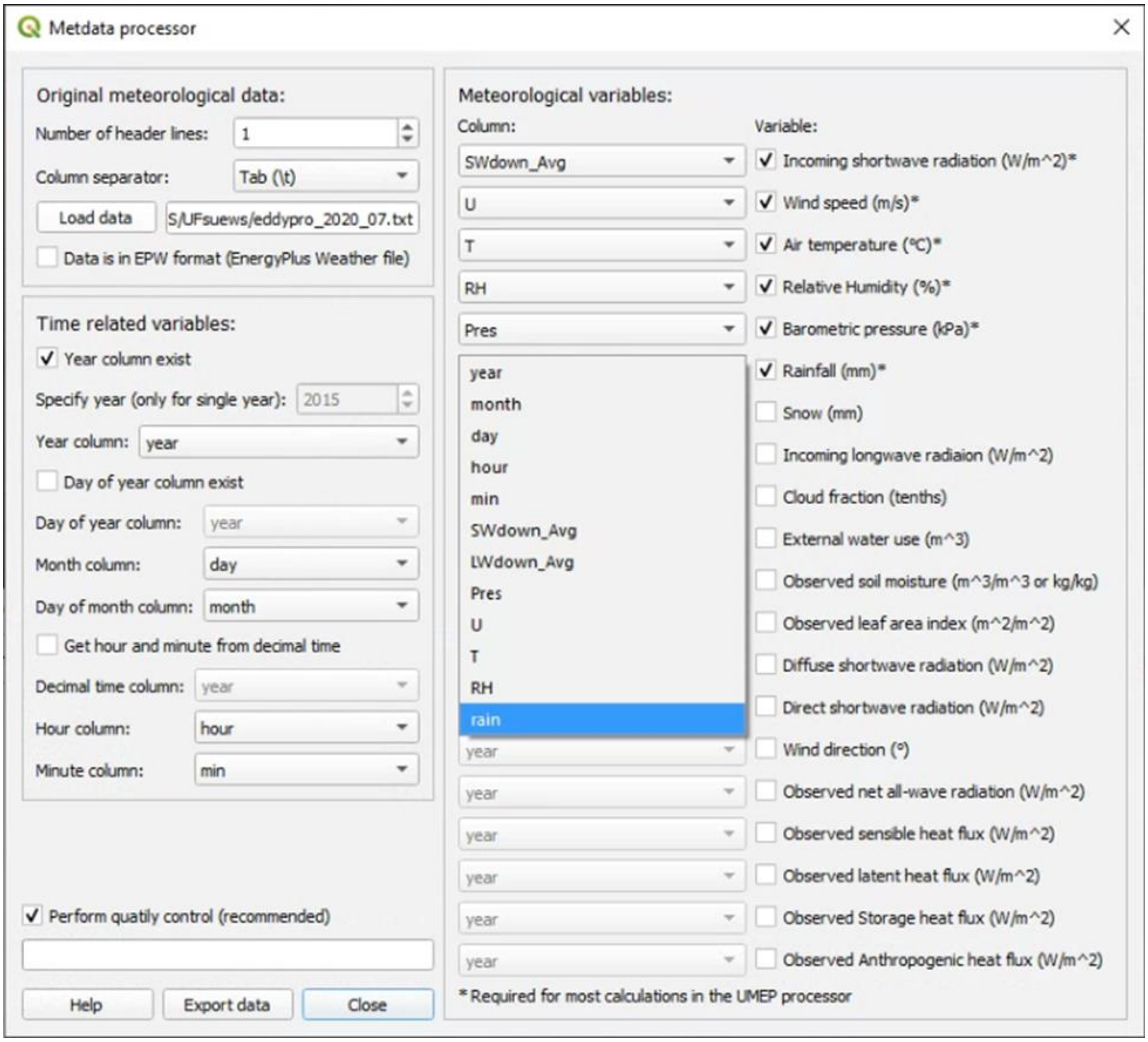

Figure 3.3 Metdata processor is the plugin that converts the meteorological data to the form that the model needed to run. Here is the User Interface of the plugin inside the QGIS program.

1. Paved surfaces (e.g. roads, car parks)
2. Buildings (Building surfaces)
3. Evergreen Trees (Evergreen trees and shrubs)
4. Deciduous Trees (Deciduous trees and shrubs)
5. Grass (Grass surfaces)
6. Bare Soil (Bare soil surfaces and unmanaged land)
7. Water (Open water (e.g. lakes, ponds, rivers, fountain))

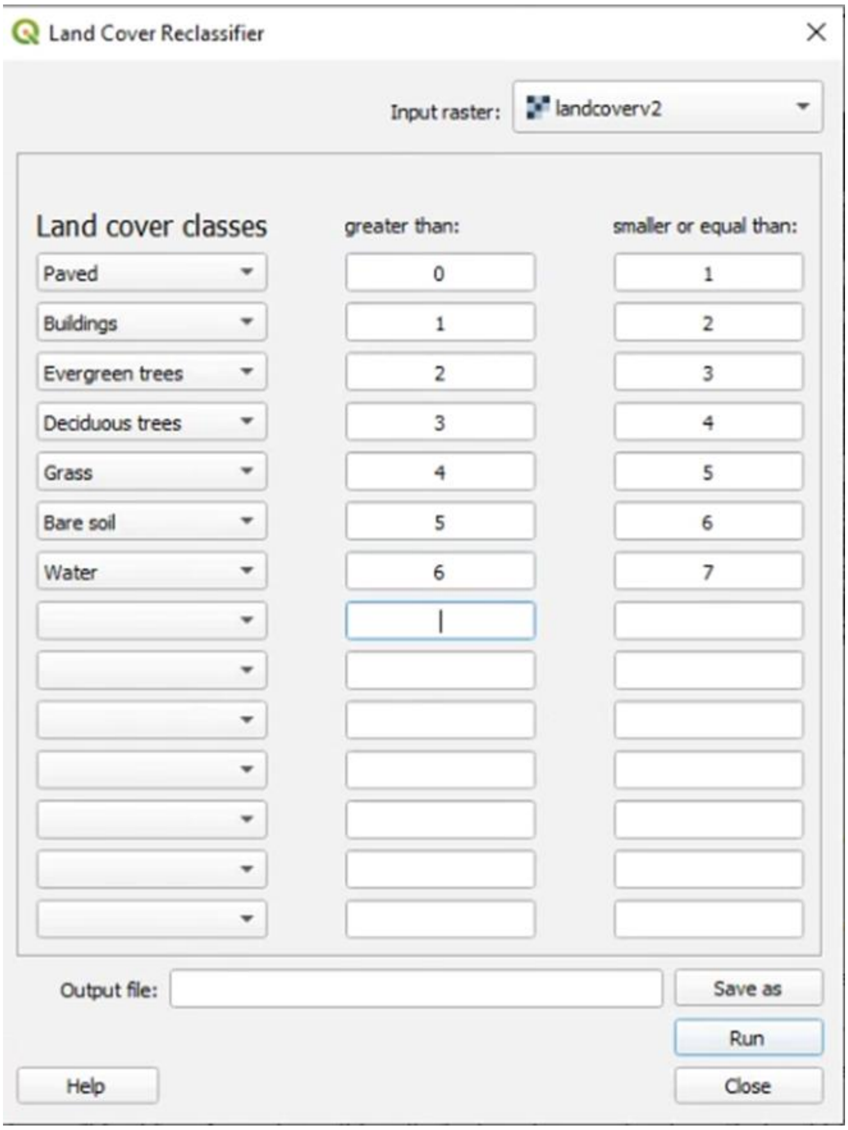

Figure 3.4 Land Cover Reclassifier is the plugin that convert the landcover to the a new one with the seven fractions for SUEWS model.

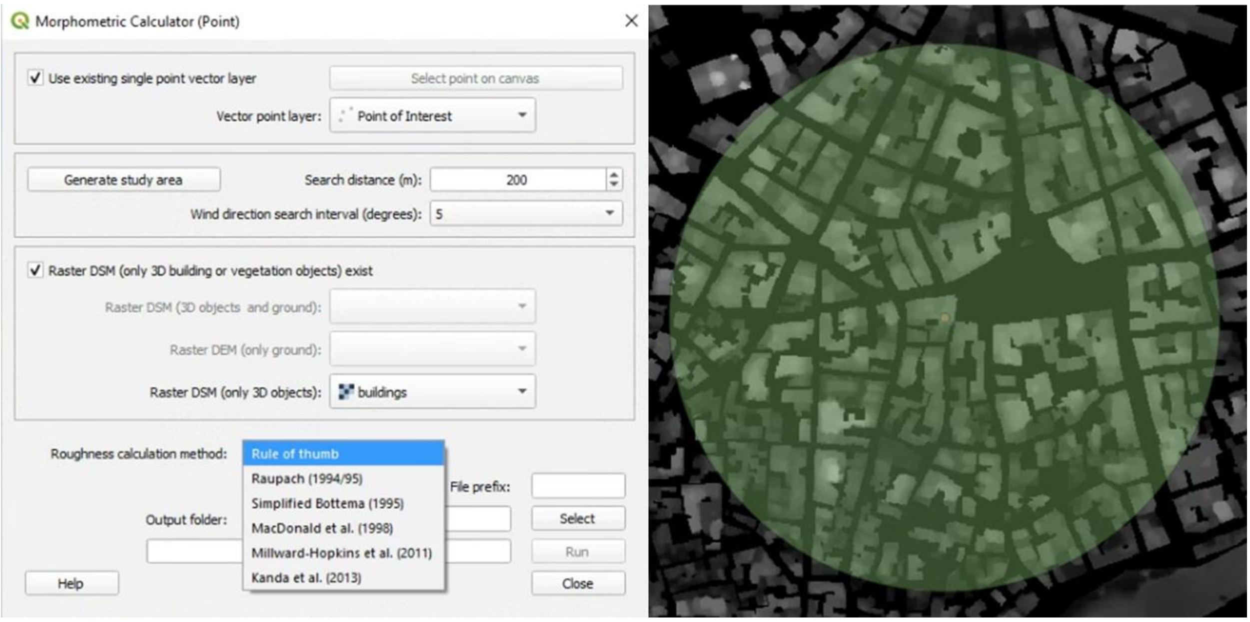

Figure 3.5 Left is the interface of Morphometric Calculator and right is the generated area with green color in 200 m radius from the center where EC tower Is installed.

The second stage of the preparation is to calculate the characteristics of the area of interest. The Morphometric Calculator (Point) plugin (Figure 3.5) calculates various morphometric parameters based on digital surface models. These morphometric parameters are used to describe the roughness of a surface and are included in various local and mesoscale climate models[76]. They may vary depending on what angle (wind direction) you are interested in. Thus, this plugin is able to derive the parameters for different directions. Preferably, a ground and 3D-object DSM or DEM and DTM should be used as input data, where DSM is the digital surface model that includes the height of the 3D objects, the DTM is the digital terrain model that includes the height of terrain below the 3D objects from the see level and DEM is the digital elevation model that includes both DSM and DTM. The 3D objects are usually buildings but can also be 3D vegetation (i.e. trees and bushes). It is also possible to derive the parameters from a 3D object DSM with no ground heights.

First a point has to be created on the canvas or imported as a vector layer as the center of the area and then the area is generated in a circle which the radius is been set and the interval in search directions for which the morphometric parameters will be calculated. Inside the Raster box the DEM and DSM are selected and then the method that roughness is calculated. The results are:

- Mean building height (Z_H), average building height measured from ground level[m]
- Standard deviation of building heights ($Z_{H\sigma}$), standard deviation of building heights [m]
- Maximum building height (Z_{Hmax}), height of the tallest building within the study area [m]
- Plan area index (λ_P) , area of building surfaces relative to the total ground area
- Frontal area index (λ_F), area of building walls normal to wind direction relative to the total ground area.
- Roughness length (Z_0), A parameter of some vertical wind profile equations that model the horizontal mean wind speed near the ground; in the log wind profile, it is equivalent to the height at which the wind speed theoretically becomes zero [m].
- Zero-plane displacement height (Z_d), Height where the ground level is theoretically displaced due to the existence of roughness objects (trees, buildings). as a result of obstacles to the flow such as trees or buildings [m].

The Land Cover Fraction (Point) plugin (Figure 3.6) calculates land cover fractions required for UMEP from a point location based on the reclassified land cover raster grid from Land Cover

Reclassifier. The fraction will vary depending on what angle (wind direction) you are interested in. Thus, this plugin is able to derive the land cover fractions for different directions.

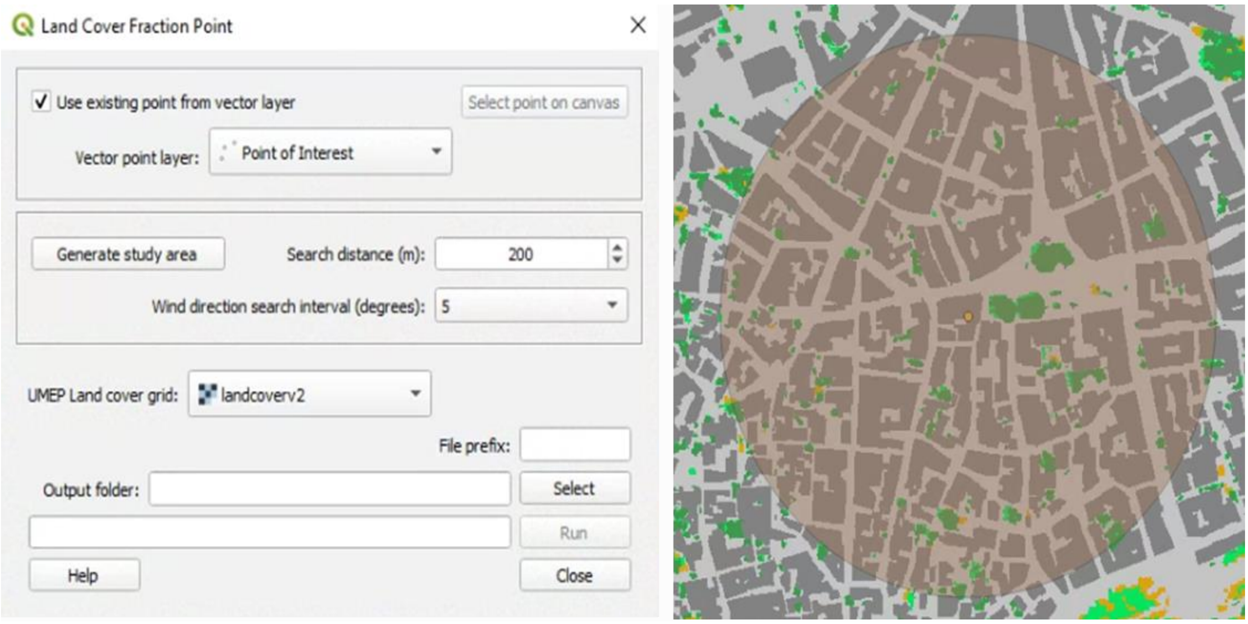

Figure 3.6 Left image is the Land Cover Fraction Point User Interface inside QGIS and the right one is the calculated area with 200m radius from the center where EC tower is installed.

3.6 Processing model

After the calculation of buildings and trees roughness, the fraction calculation and the conversion of meteorological data, the model can be run using the prepared data. The plugin has four boxes, Building morphology, Tree morphology, Land Cover fraction and Initial conditions. Inside the Buildings/Tree morphology and Land cover fractions there are two options, fetch file and Open tool to generate. Using fetch file, the generated files from pre-processing stage can be selected to import the values. Using the open tool to generate, the Morphometric tool and Land Cover Fraction are open to generate the values. Also, the values inside the boxes can be customized to test hypothetical scenarios. The initial conditions can be set inside the box of Initial conditions.

Some more data that are necessary to run are the following:

- Year
- Latitude
- Longitude
- Population Density
- UTC offset
- Height of the meteorological station from the ground

these parameters have to be completed in the User Interface of the plugin inside QGIS as it is shown in Figure 3.7. After the complete run of the model some plots appear if the option “Show basic plots of model Results” is checked. The first plot (Figure 3.8) includes monthly partition of energy surface balance and the monthly water balance and the second plot (Figure 3.9) includes the radiation fluxes, energy fluxes, and water related outputs.

The output files are text files with the results for variables in columns and time in raw. The output text can be used to create plots for the values. SUEWS produces the main output file (SSss_YYYY_SUEWS_tt.txt) with time resolution (TT min) set by ResolutionFilesOut in RunControl.nml. The variables included in the main output file (Table 3-4) are determined according to WriteOutOption(Table 3-3) set in RunControl.nml

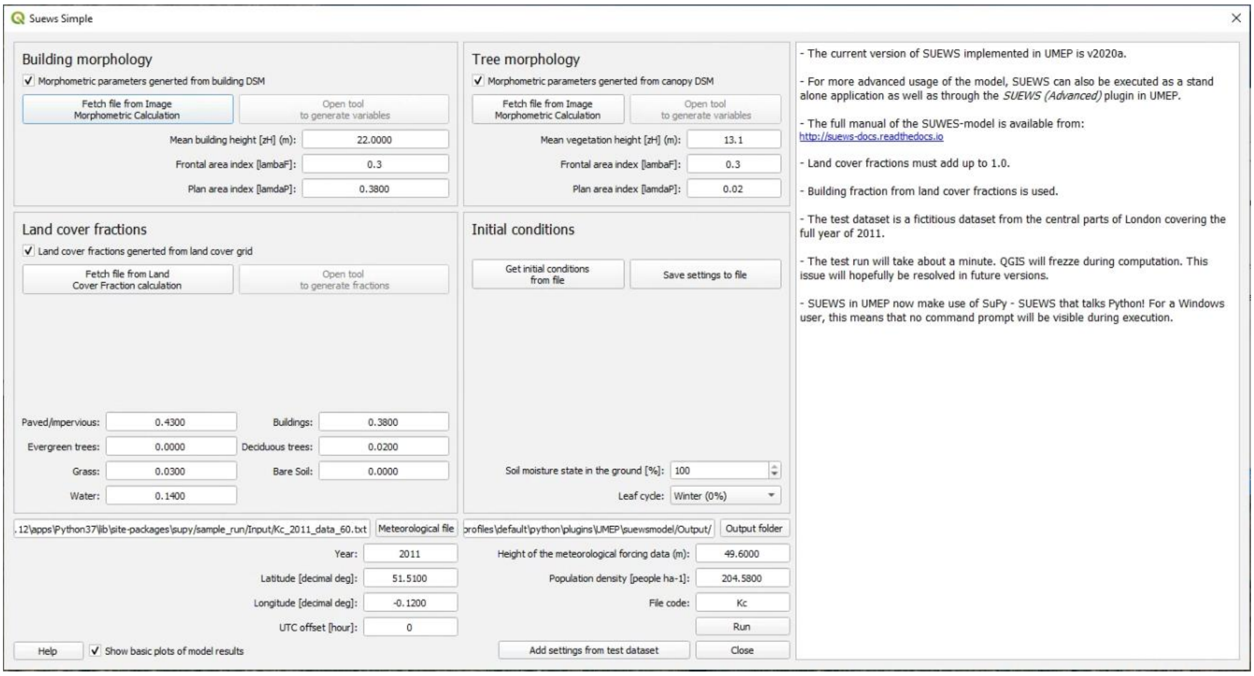

Figure 3.7 The User Interface of the model.

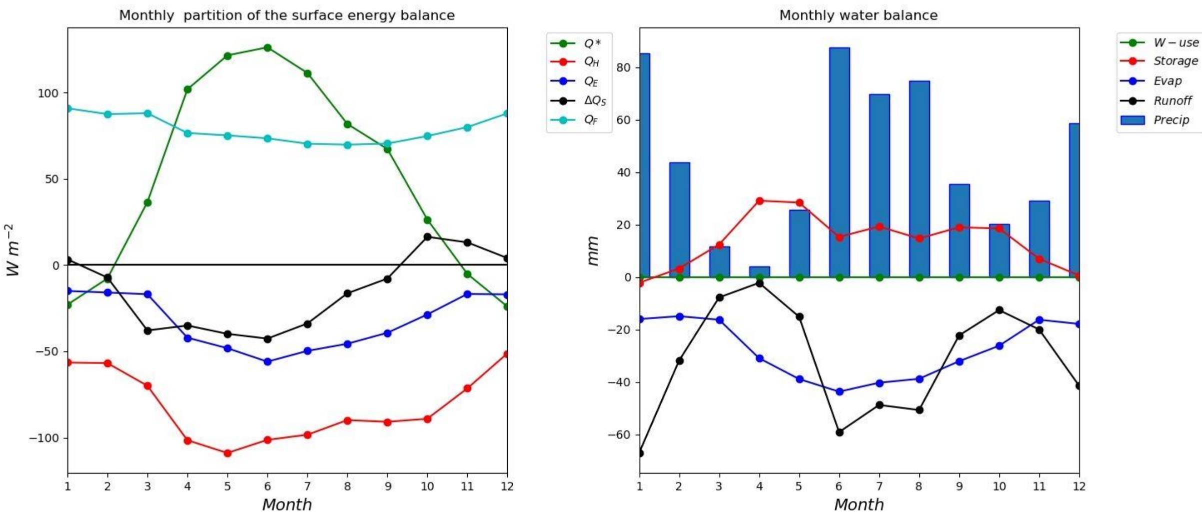

Figure 3.8 Left graph is the monthly partition of energy surface balance and the left is the monthly water balance as it is created automatic finishing the run. The plots are from test data that are included in the program.

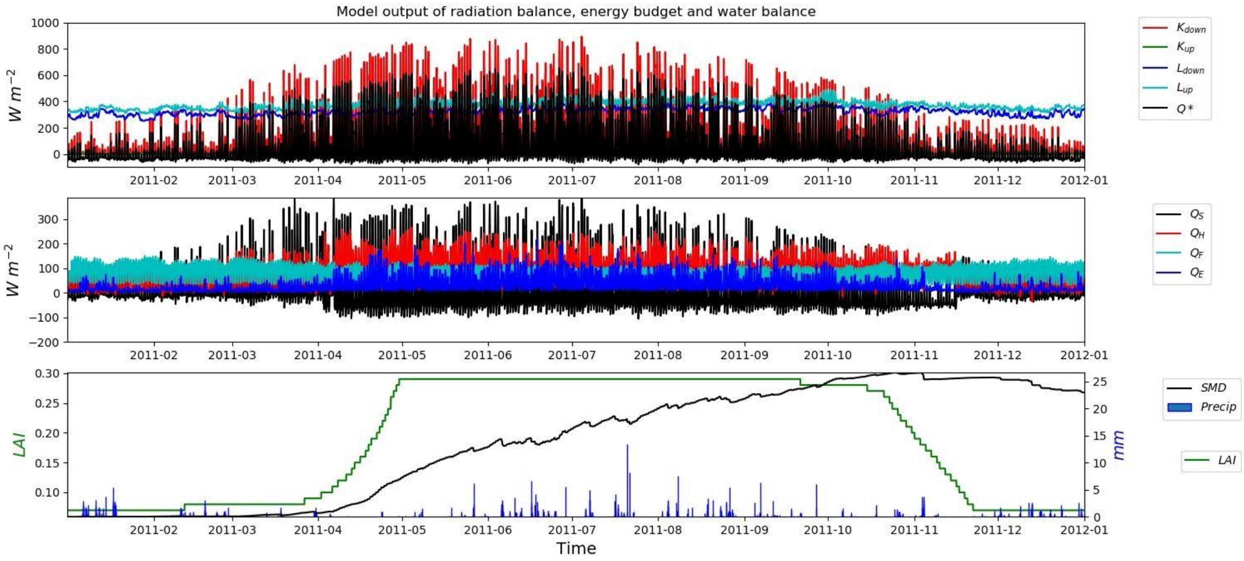

Figure 3.9 Top diagram is the net-wave radiations, the middle one is the energy fluxes and the bottom one is the water related outputs. The plots are from test data that are included in the program.

Table 3-3. WriteOutOption Specifies which variables are written in the output files.	
Value	Comments
0	All (except snow-related) output variables written. This is the default option.
1	All (including snow-related) output variables written.
2	Writes out a minimal set of output variables (use this to save space or if information about the different surfaces is not required).

Table 3-4. Variables included in the main output file.

Column	Name	WriteOutOption	Description
1	Year	0,1,2	Year [YYYY]
2	DOY	0,1,2	Day of year [DOY]
3	Hour	0,1,2	Hour [H]
4	Min	0,1,2	Minute [M]
5	Dectime	0,1,2	Decimal time [-]
6	Kdown	0,1,2	Incoming shortwave radiation [W m^{-2}]
7	Kup	0,1,2	Outgoing shortwave radiation [W m^{-2}]
8	Ldown	0,1,2	Incoming longwave radiation [W m^{-2}]
9	Lup	0,1,2	Outgoing longwave radiation [W m^{-2}]
10	Tsurf	0,1,2	Bulk surface temperature [°C]
11	QN	0,1,2	Net all-wave radiation [W m^{-2}]
12	QF	0,1,2	Anthropogenic heat flux [W m^{-2}]
13	QS	0,1,2	Storage heat flux [W m^{-2}]
14	QH	0,1,2	Sensible heat flux (calculated using SUEWS) [W m^{-2}]
15	QE	0,1,2	Latent heat flux (calculated using SUEWS) [W m^{-2}]
16	QHlumps	0,1	Sensible heat flux (calculated using LUMPS) [W m^{-2}]
17	QElumps	0,1	Latent heat flux (calculated using LUMPS) [W m^{-2}]
18	QHresis	0,1	Sensible heat flux (calculated using resistance method) [W m^{-2}]
19	Rain	0,1,2	Rain [mm]
20	Irr	0,1,2	Irrigation [mm]
21	Evap	0,1,2	Evaporation [mm]
22	RO	0,1,2	Runoff [mm]
23	TotCh	0,1,2	Change in surface and soil moisture stores [mm]
24	SurfCh	0,1,2	Change in surface moisture store [mm]
25	State	0,1,2	Surface wetness state [mm]
26	NWtrState	0,1,2	Surface wetness state (for non-water surfaces) [mm]
27	Drainage	0,1,2	Drainage [mm]
28	SMD	0,1,2	Soil moisture deficit [mm]

29	FlowCh	0,1	Additional flow into water body [mm]
30	AddWater	0,1	Additional water flow received from other grids [mm]
31	ROSoil	0,1	Runoff to soil (sub-surface) [mm]
32	ROPipe	0,1	Runoff to pipes [mm]
33	ROImp	0,1	Above ground runoff over impervious surfaces [mm]
34	ROVeg	0,1	Above ground runoff over vegetated surfaces [mm]
35	ROWater	0,1	Runoff for water body [mm]
36	WUInt	0,1	Internal water use [mm]
37	WUEveTr	0,1	Water use for irrigation of evergreen trees [mm]
38	WUDecTr	0,1	Water use for irrigation of deciduous trees [mm]
39	WUGrass	0,1	Water use for irrigation of grass [mm]
40	SMDPaved	0,1	Soil moisture deficit for paved surface [mm]
41	SMDBldgs	0,1	Soil moisture deficit for building surface [mm]
42	SMDEveTr	0,1	Soil moisture deficit for evergreen surface [mm]
43	SMDDecTr	0,1	Soil moisture deficit for deciduous surface [mm]
44	SMDGrass	0,1	Soil moisture deficit for grass surface [mm]
45	SMDBSoil	0,1	Soil moisture deficit for **bar**e soil surface [mm]
46	StPaved	0,1	Surface wetness state for paved surface [mm]
47	StBldgs	0,1	Surface wetness state for building surface [mm]
48	StEveTr	0,1	Surface wetness state for evergreen tree surface [mm]
49	StDecTr	0,1	Surface wetness state for deciduous tree surface [mm]
50	StGrass	0,1	Surface wetness state for grass surface [mm]
51	StBSoil	0,1	Surface wetness state for **bar**e soil surface [mm]
52	StWater	0,1	Surface wetness state for water surface [mm]
53	Zenith	0,1,2	Solar zenith angle [°]
54	Azimuth	0,1,2	Solar azimuth angle [°]
55	AlbBulk	0,1,2	Bulk albedo [-]
56	Fcld	0,1,2	Cloud fraction [-]
57	LAI	0,1,2	Leaf area index [m 2 m^{-2}]
58	z0m	0,1	Roughness length for momentum [m]
59	zdm	0,1	Zero-plane displacement height [m]

60	ustar	0,1,2	Friction velocity [m s^{-1}]
61	Lob	0,1,2	Obukhov length [m]
62	RA	0,1	Aerodynamic resistance [s m^{-1}]
63	RS	0,1	Surface resistance [s m^{-1}]
64	Fc	0,1,2	CO2 flux [umol m^{-2} s^{-1}]
65	FcPhoto	0,1	CO2 flux from photosynthesis [umol m^{-2} s^{-1}]
66	FcRespi	0,1	CO2 flux from respiration [umol m^{-2} s^{-1}]
67	FcMetab	0,1	CO2 flux from metabolism [umol m^{-2} s^{-1}]
68	FcTraff	0,1	CO2 flux from traffic [umol m^{-2} s^{-1}]
69	FcBuild	0,1	CO2 flux from buildings [umol m^{-2} s^{-1}]
70	FcPoint	0,1	CO2 flux from point source [umol m^{-2} s^{-1}]
71	QNSnowFr	1	Net all-wave radiation for snow-free area [W m^{-2}]
72	QNSnow	1	Net all-wave radiation for snow area [W m^{-2}]
73	AlbSnow	1	Snow albedo [-]
74	QM	1	Snow-related heat exchange [W m^{-2}]
75	QMFreeze	1	Internal energy change [W m^{-2}]
76	QMRain	1	Heat released by rain on snow [W m^{-2}]
77	SWE	1	Snow water equivalent [mm]
78	MeltWater	1	Meltwater [mm]
79	MeltWStore	1	Meltwater store [mm]
80	SnowCh	1	Change in snow pack [mm]
81	SnowRPaved	1	Snow removed from paved surface [mm]
82	SnowRBldgs	1	Snow removed from building surface [mm]
83	Ts	0,1,2	Skin temperature [°C]
84	T2	0,1,2	Air temperature at 2 m agl [°C]
85	Q2	0,1,2	Air specific humidity at 2 m agl [g kg^{-1}]
86	U10	0,1,2	Wind speed at 10 m agl [m s^{-1}]
87	RH2	0,1,2	Relative humidity at 2 m agl [%]

4 MODEL EVALUATION

4. Model evaluation

The model evaluation is focusing on the local/ neighborhood scale fluxes at 100m radius around the location of the EC tower for the month of July 2018. The evaluation area is defined by the green dotted line in Figure 3.1. The EC observation source area depends on the wind speed, direction and stability [71], while the origination area of the EC fluxes is calculated from the footprint model a few hundred meters of the flux tower. The upwelling source area of EC outlines are depicted in white color (60%,70%,80%,90%) and the radiometer isopleth is marked with the orange circle (Figure 3.1).

SUEWS model is running offline with 5 min time-step. The resolution of the various meteorological data that are required for the model is 60 min. A linear interpolation is performed in a 5 min interval for all data apart from precipitation that is considered constant for 60 min. The outputs of the model are averaged to 60 min to be comparable with the obtained observational data[3]. The indicated evaluation area is selected to match with the source area of radiometer for Q*[77] and the footprint of urban turbulent fluxes (Figure 3.1). The model evaluation is performed using the data collected from the CNR1 radiometer and the EC tower. The variables that are used for the model evaluation are all radiation variables and the turbulent sensible heat flux. Root Mean Square Error (RMSE) and coefficient of determination (R^2) are used for the comparison of the modeled versus the measured variables.

The evaluation results for each variable are discussed in the following sub-sections.

4.1 Net all wave radiation

The measured vs modeled $K_{\downarrow}$, $K_{\uparrow}$, $L_{\downarrow}$, $L_{\uparrow}$ are depicted in Figure 4.1. The net all-wave radiation evaluation results are depicted in Figure 4.2. The Q* model approximation is very high with R^2 reaching 0.99 and a scatter that is really small (RMSE= 54 W m^{-2}). The errors of $L_{\downarrow}$ and $K_{\uparrow}$ are those that mostly affect the differences of modeled versus measured Q*. The underestimation of $K_{\uparrow}$ is due to the area structure of radiometers footprint so the radiometer also has an error from the real reflected short-wave radiation. The error of $L_{\downarrow}$ is due to miscalculation of the cloud cover, using the $L_{\downarrow}$ observational data Q* could be improved. It is important that simulation results have the same behavior with observational data as the purpose of the study is to investigate the behavior of different scenarios in the surrounding area of urban and sub-urban environments (Figure 4.1).

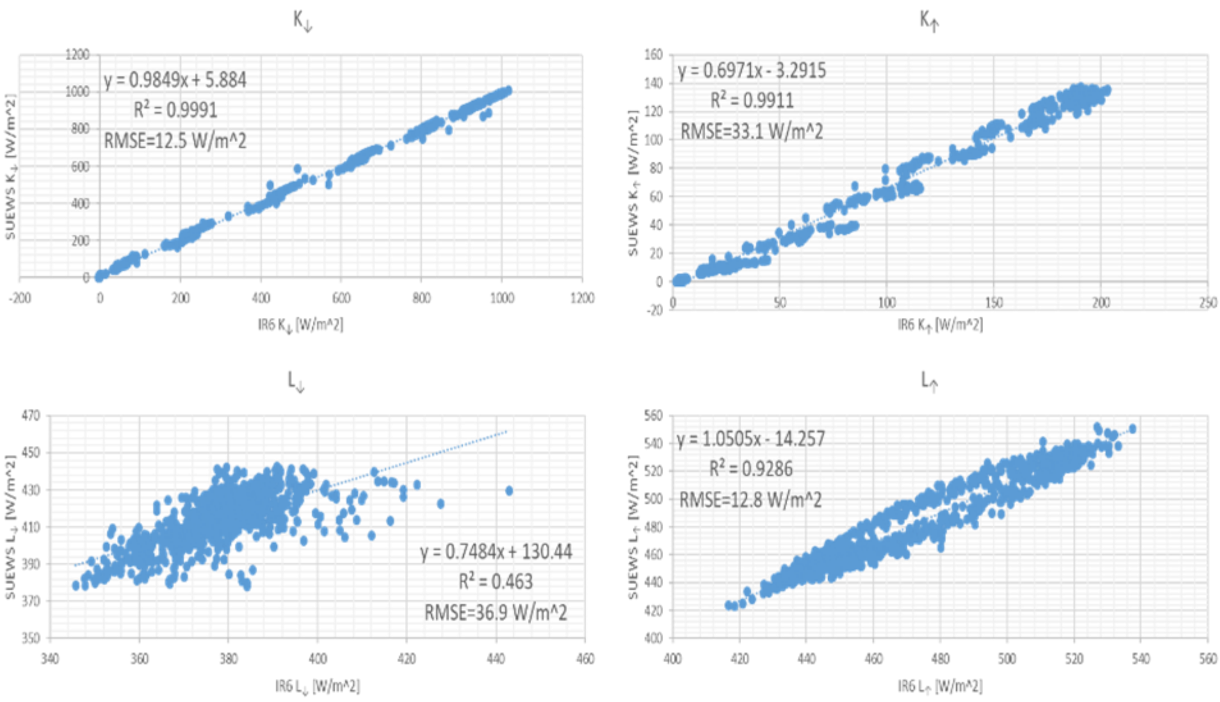

Figure 4.1 Modeled radiations by SUEWS versus observed from CNR1 sensor.

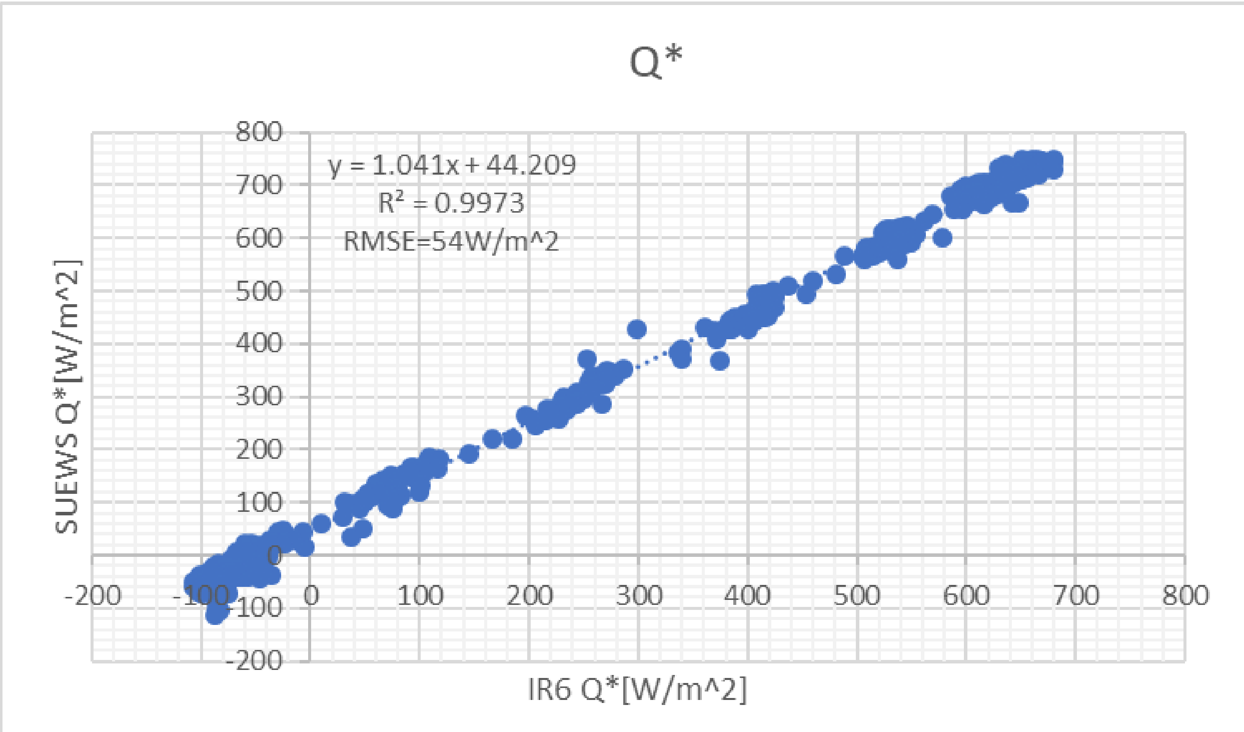

Figure 4.2 Modeled Q from SUEWS versus IR6 calculated Q*. The high R^2 means that the relationship of the products is depicted by the observational data curve*

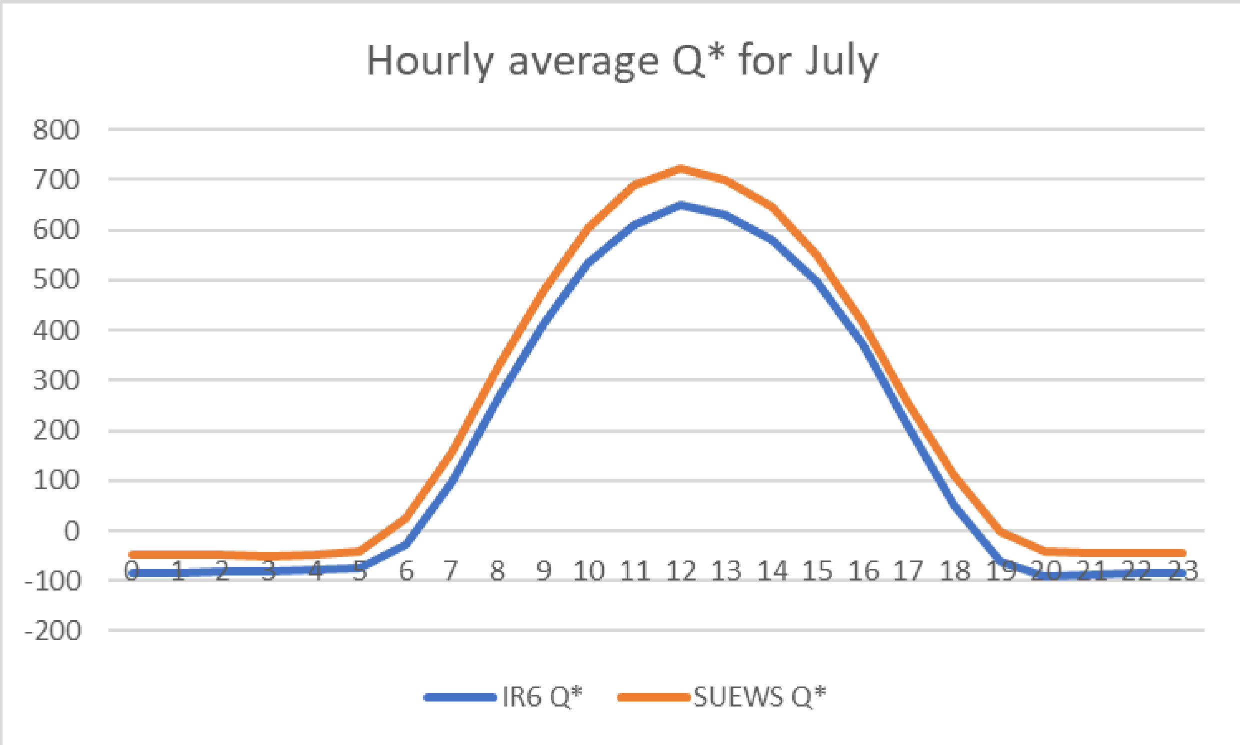

Figure 4.3 Hourly average Q for the month of July. There is a small overestimation for every hour of the day but still have the same scheme. As the albedo is not exactly the same for the reason that we mentioned before.*

The Q*overestimation (Figure 4.3) is attributed to the following factors:

- The existence of street canyons in the larger source area of the CNR1 radiometer affects the overall bulk albedo which sees mainly roof surface and due to different materials that are used to the area (≈0.2) [78]. The model used average albedo of the whole area for the calculation of the albedo that does not include the morphology of the area. The lack of optical interaction between paved and CNR1 radiometer overestimates the observational albedo [3].

The CNR1 radiometer is installed in a site to provide radiative fluxes that represent the EC footprint. On the other hand, the EC footprint is dynamic and depends on the characteristics of the site and meteorological conditions (wind, etc.) instead of the radiometers source area that is much smaller and constant in time and space.

4.2 Sensible heat flux

The monitored versus modeled turbulent sensible heat flux is depicted in Figure 4.4. Turbulent sensible Heat flux is calculated as the residual of energy balance. Therefore, the error of each one heat flux is accumulated to turbulent sensible heat flux. The RMSE is 61.36 W m^{-1}, which is reasonable due to error propagation and the irregular source area of the EC that changes by time according to the wind speed, wind direction, atmospheric stability and lateral dispersion qualities of the flow[71].

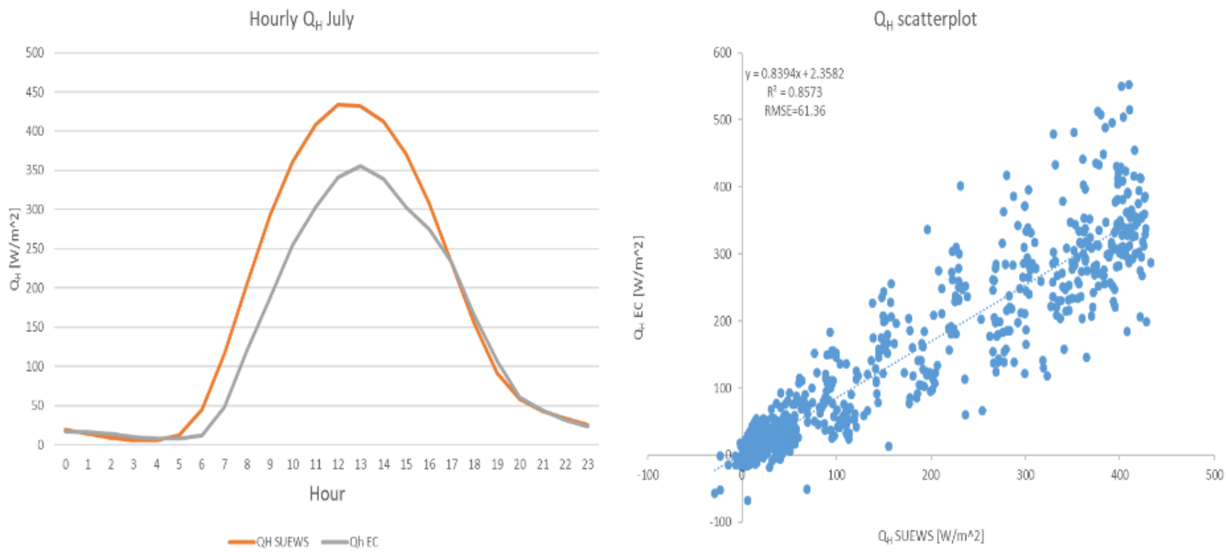

Figure 4.4 The hourly average of Q_H for the month of July on the left and the sensible heat flux.

4.2.1 Latent heat flux

The turbulent latent heat flux is modeled using the equation 10. The pattern of the calculated turbulent latent heat flux is following the pattern of the measured turbulent latent heat flux. The RMSE error is very high compared to the absolute values, 55.9 W/m^2, due to the inability of the model to simulate the large number of hourly fluctuations that includes high range peaks as a result the overestimation or underestimation of turbulent latent heat flux from the model.

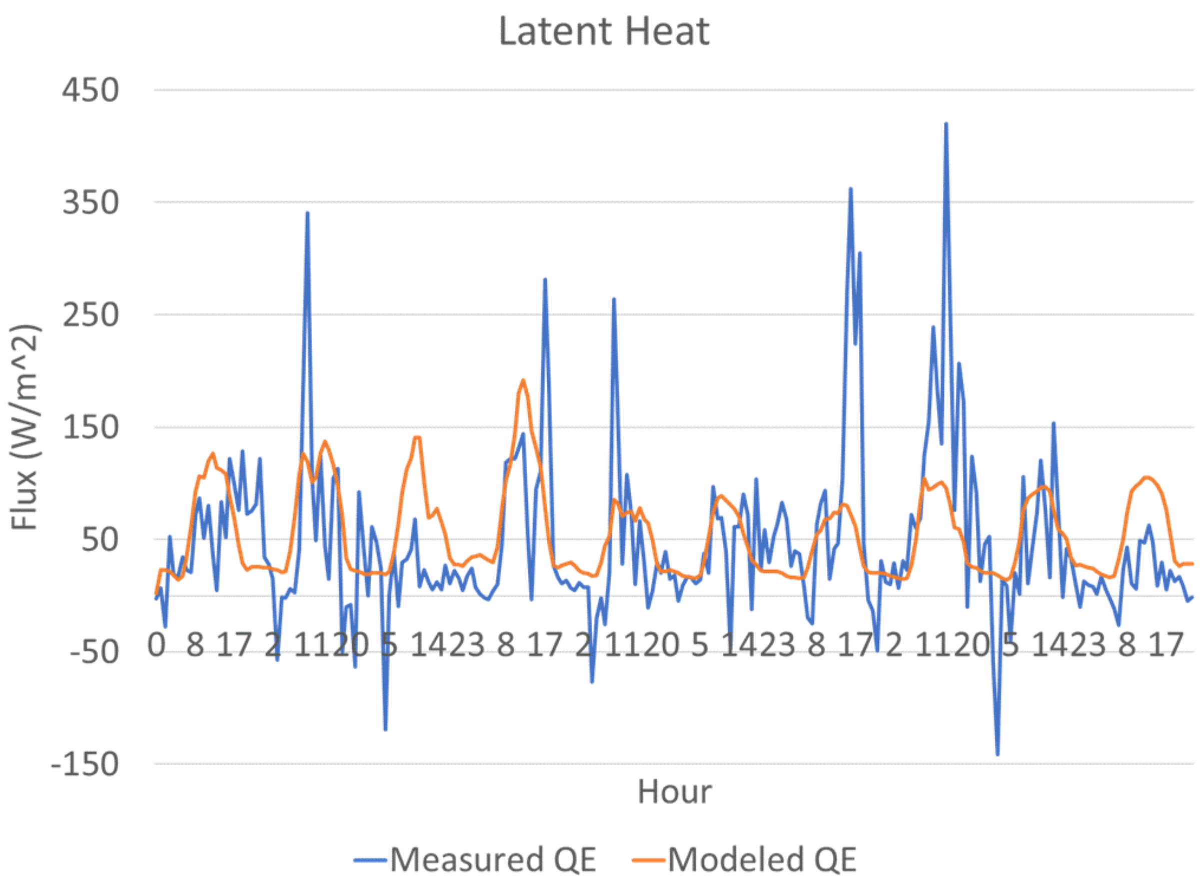

Figure 4.5 The turbulent latent heat flux for 9 days of July

5 RESULTS

5. Results and Discussion

Following the SUEWS model development and evaluation for Heraklion, the evaluated model is utilized to analyze the impact of NBS on the specific urban area. The NBS that are proposed are mainly linked with greenery and water bodies development. Five different NBS scenarios are simulated and studied:

1. Replacement of pavements with trees
2. Replacement of roofs with grass
3. Replacement of pavements with grass
4. Mixture of replacement of roofs with grass and pavements with trees
5. Replacement of pavements with water bodies

Using these solutions, the evaporation and the albedo of the city area is changed leading to changes of the energy fluxes. Increasing the green areas of the city, the turbulent latent heat flux increases and turbulent sensible heat flux decreases leading to evaporative cooling due to evapotranspiration. Also, changing the albedo of the area, affects the reflected radiation that could lead in radiative cooling by using cool materials. In this study the change of the radiation heat flux is negligible due to small difference between paved, building, grass and trees so the study focuses in evaporative cooling. The changes of energy fluxes have a direct impact on the air temperature and relative humidity at 2m height above ground that calculated from the model using initial data from the station that collected from 27m above the ground. (see Figure 2.2). The changes are discussed in the following subsections.

5.1 Replacement of pavements with trees

In the specific scenario the surface cover fractions are changed versus the baseline conditions tabulated in Table 3-1. Three different conditions are examined where different fractions are analyzed, i.e. 10% and 20% increase of trees. The type of trees used are deciduous trees.

The changes of air temperature in 2m height in the simulation area when replacing pavements with trees is depicted in Figure 5.1. The specific figure illustrates the air temperature for two days during summer period where the urban overheating is present. By replacing the existing pavements with deciduous trees, a reduction of air temperature occurs during daytime. As depicted in Figure 5.1 the air temperature when trees are inserted peaks faster than baseline before midday instead of baseline scenario that temperature exceeds the trees scenario after midday. The maximum air temperature difference which is almost 0.5K is found for 20% replacement of pavements. The overall changes on monthly basis and during daytime are tabulated Table 5-1. We notice that there is a decrease of Q^* due to the increase of surface albedo of deciduous trees (see Table 2-1) versus the pavements for summer months. Moreover, there is a decrease of turbulent sensible heat flux from the city to the atmosphere (Q_H) about 150 to 200 W/m^2 depending on the period (Figure 5.2) due to the changes of the other fluxes as explained in Eq. 12. An increase of the turbulent latent heat flux (Figure 5.3), that is almost equal to the decrease of sensible heat flux, indicates increase of evapotranspiration around the trees and increase of the relative humidity in the air. The change of the relative humidity is quite significant and reaches 23.5% increase when 20% of pavements are replaced with deciduous trees.

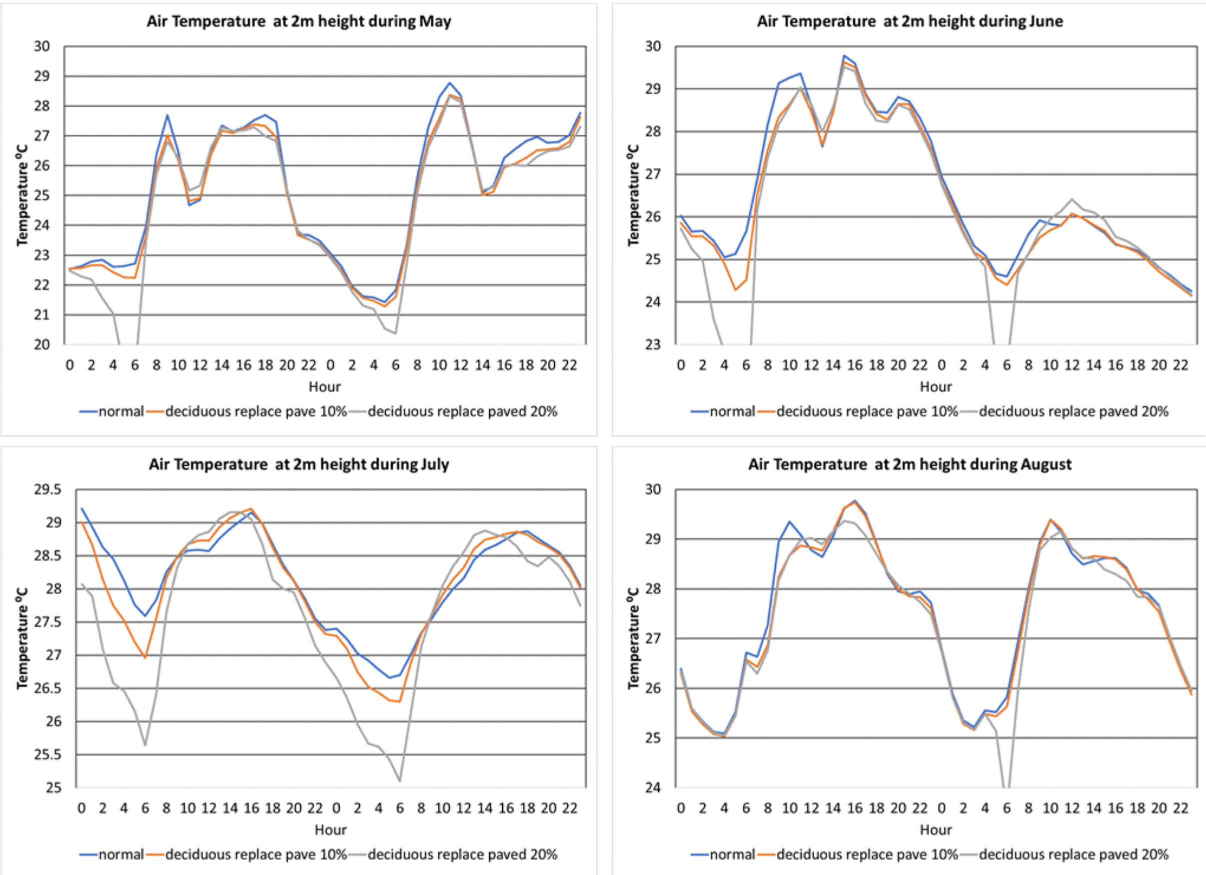

Figure 5.1 Air temperature for 2 days during May, June, July and August for the replacement of pavements with trees.

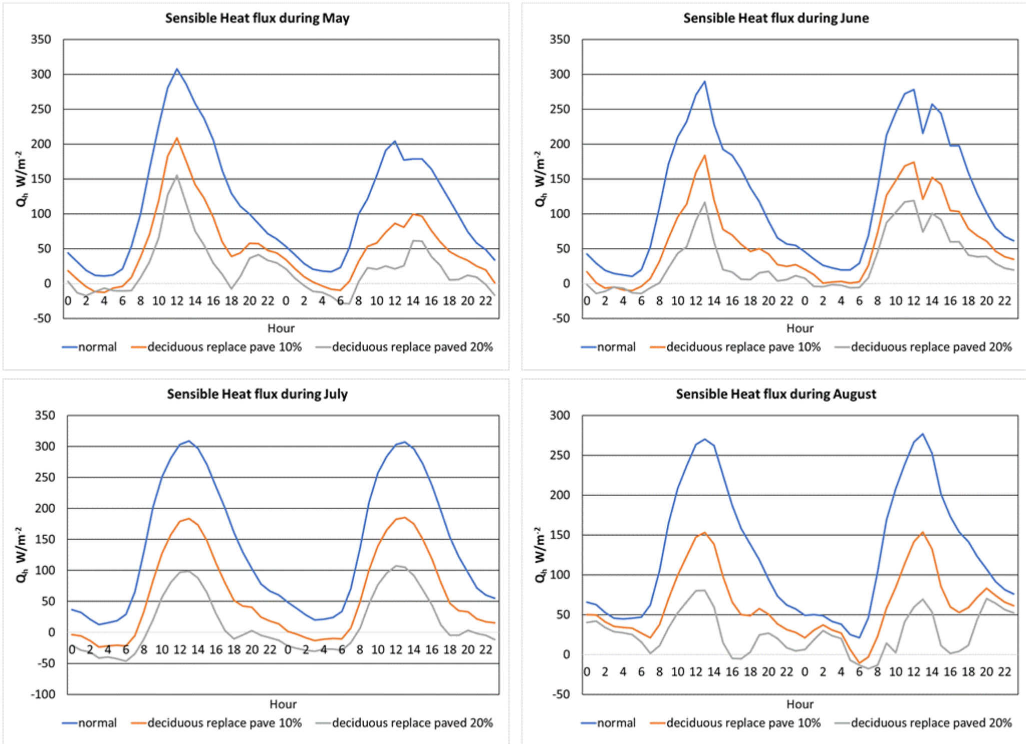

Figure 5.2 Sensible heat flux for 2 days during May, June, July and August for the replacement of pavements with trees

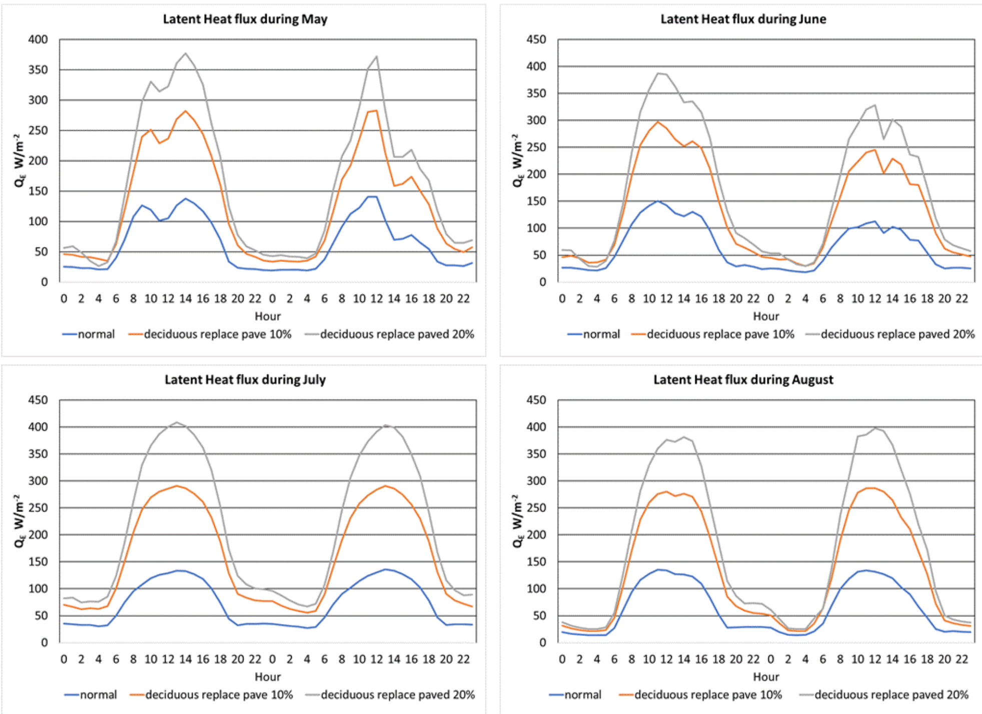

Figure 5.3 Turbulent Latent heat flux for 2 days during May, June, July and August for the replacement of pavements with trees.

Table 5-1. Percentage of changes for all fluxes and for air temperature and relative humidity during daytime on monthly basis for the replacement of pavements with trees.						
Month	Deciduous green trees replace pavements 10%					
	Q^*	ΔQ_s	Q_H	Q_E	T_{air}	RH
May	-0.88%	-4.51%	-191.44%	103.80%	-0.25%	4.24%
June	-0.95%	-4.43%	-84.07%	106.27%	-0.47%	6.07%
July	-3.75%	-16.92%	-58.72%	104.49%	-0.38%	5.23%
August	-1.16%	-2.21%	-63.96%	108.62%	-0.10%	3.40%
	Deciduous green trees replace pavements 20%					
	Q^*	ΔQ_s	Q_H	Q_E	T_{air}	RH
May	-1.79%	-8.84%	-329.88%	162.70%	-0.30%	13.56%
June	-1.89%	-8.56%	-120.15%	163.74%	-1.20%	23.54%
July	-9.82%	-33.28%	-90.28%	162.25%	-0.77%	18.03%
August	-3.36%	-4.30%	-100.24%	169.45%	-0.62%	14.08%

5.2 Replacement of roofs with green roofs

The roofs of the city area of Heraklion are replaced with green roofs. In order to simulate this scenario, the concrete roofs are replaced with grass. Three different fractions are examined in this scenario, i.e. 10%, 20% and 30% replacement of roofs' area with grass.

The replacement of roofs with grass reduces the Q^* since the surface albedo is increased (Table 2-1). Moreover, the changes of air temperature at 2m height are illustrated in Figure 5.4 showing a significant decrease for this scenario that during daytime can reach up to 1-1.5K. This is also tabulated in Table 4 where for all daytime during May there is a decrease of air temperature of 0.8% while in July and August this percentage reaches 2.2% and 1.8 respectively. The highest decrease is pinpointed when a 30% increase of grass is performed. Again, the increase of the turbulent latent heat flux (Figure 5.6) is present in this scenario, from 150W/m^2 for May to 350 W/m^2 for July for the scenario of changing 10% of grass, this difference increases along with the increase of grass area, while a significant increase of relative humidity is noticed that can reach 33.32%. Again, the sensible heat flux decreases (Figure 5.5) almost the same amount of energy that turbulent latent heat flux increases (Figure 5.6) ≈350 W/m^2 for the 30% replacement scenario during July.

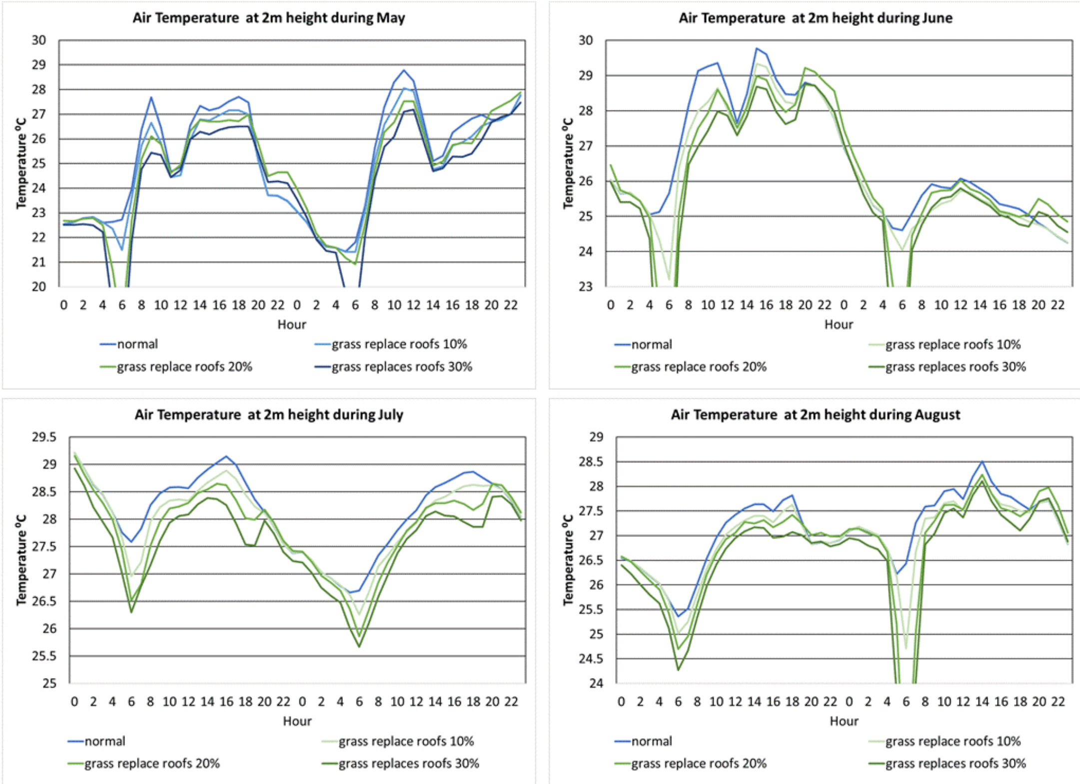

Figure 5.4 Air temperature for 2 days during May, June, July and August for the replacement of roofs with green roofs

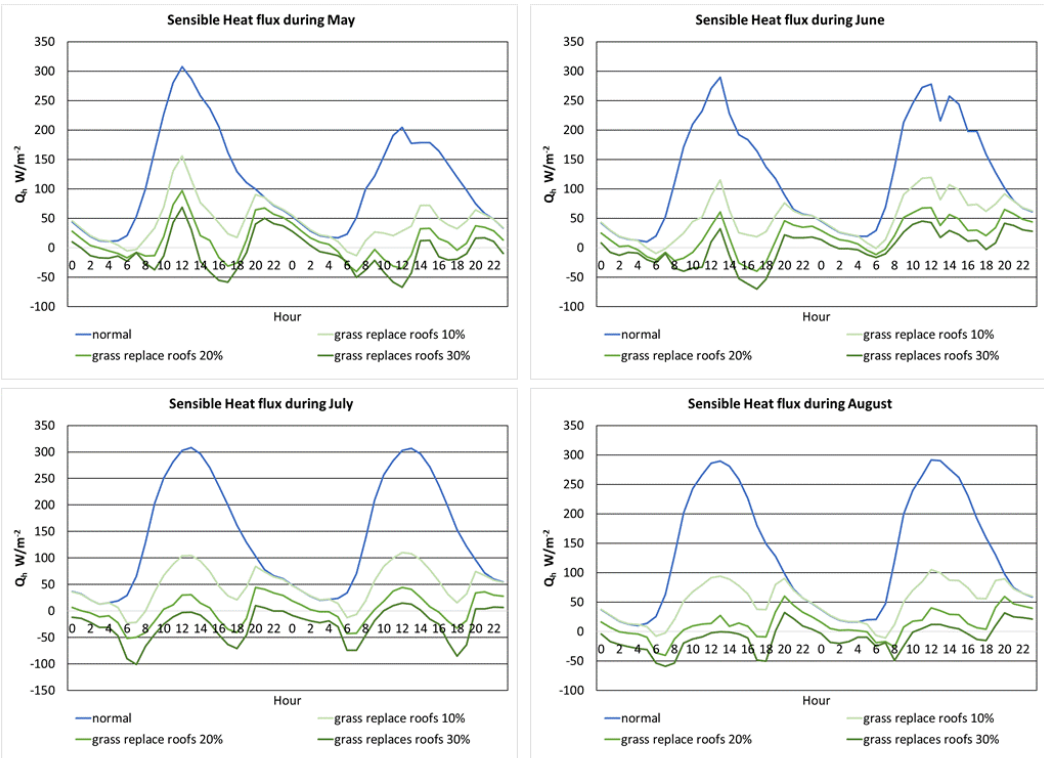

Figure 5.5 Sensible heat flux for 2 days during May, June, July and August for the replacement of roofs with green roofs.

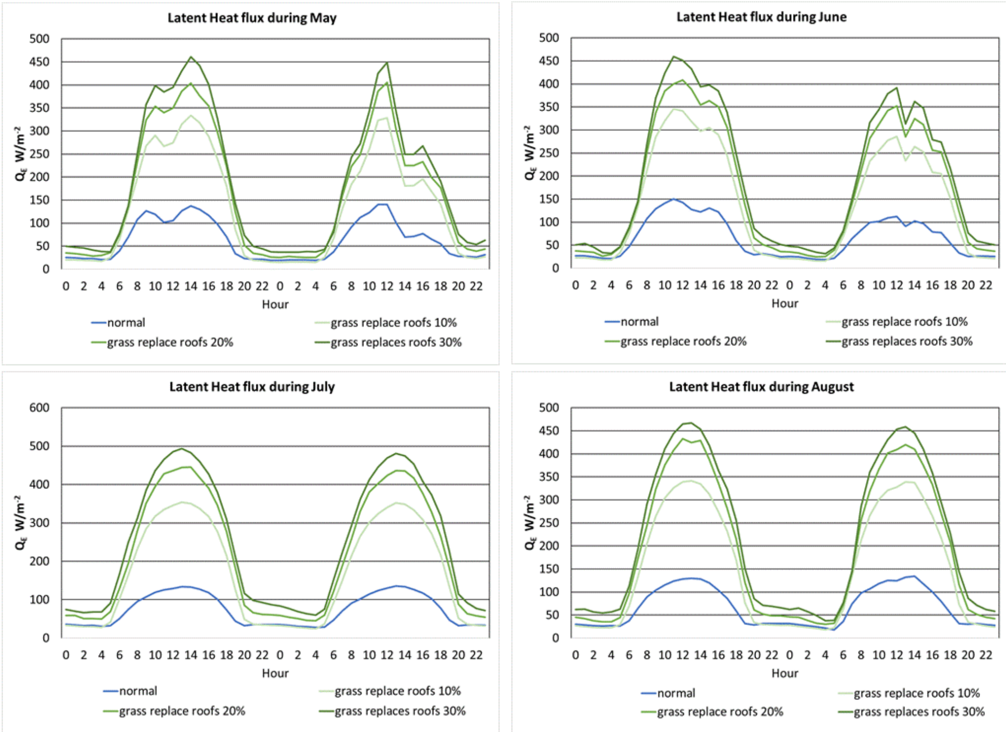

Figure 5.6 Turbulent latent heat flux for 2 days during May, June, July and August for the replacement of roofs with green roofs.

Table 5-2. Percentage of changes for all fluxes and for air temperature and relative humidity during daytime on monthly basis for the replacement of roofs with grass.

Month	Green roofs replace existing roofs 10%					
	Q*	ΔQs	QH	QE	Tair	RH
May	-1.12%	-2.73%	-32.90%	70.37%	-0.68%	3.81%
June	-1.10%	-3.20%	-52.12%	81.92%	-0.94%	6.91%
July	-4.32%	-9.75%	-44.78%	79.99%	-0.84%	5.67%
August	-1.35%	-1.40%	-43.09%	79.90%	-0.52%	3.07%
	Green roofs replace existing roofs 20%					
	Q*	ΔQs	QH	QE	Tair	RH
May	-2.25%	-5.32%	-145.35%	141.49%	0.43%	11.79%
June	-2.20%	-6.20%	-105.34%	143.42%	-0.85%	21.85%
July	-8.58%	-19.14%	-77.79%	139.11%	-0.64%	16.78%
August	-2.83%	-2.71%	-81.23%	143.33%	-0.57%	11.67%
	Green roofs replace existing roofs 30%					
	Q*	ΔQs	QH	QE	Tair	RH

May	-3.37%	-7.78%	-303.30%	193.89%	-0.83%	19.01%
June	-3.30%	-8.99%	-142.67%	187.28%	-2.22%	32.07%
July	-12.85%	-28.11%	-102.26%	182.29%	-1.82%	24.62%
August	-4.31%	-3.94%	-109.92%	188.83%	-1.62%	18.69%

5.3 Replacement of pavements with grass

In this specific scenario three alternatives are examined, i.e. 10%, 20% and 30% replacement of pavements with grass. The impact of replacement of pavement to grass on the air temperature is depicted in Figure 5.7 Air temperature for 2 days during May, June, July and August for the replacement of pavements with grass. The decrease of air temperature reaches almost 1K for 30% replacement of grass for the month of July. The decrease of Q_H (Figure 5.8) is attributed to the overall balance of the fluxes based on Eq. 12 and it is mainly due to the significant increase of the turbulent latent heat flux and the decrease of the net wave radiation for the box of Figure 2.2. Again, the results are similar to previous case of replacing roofs with grass, the turbulent latent heat flux increases between 100 and 200 W/m^2 proportionally to the replacement of grass (Figure 5.8) and the sensible heat is decreased between 200 and 350 W/m^2 (Figure 5.9). In almost all cases a slight increase of relative humidity is noticed.

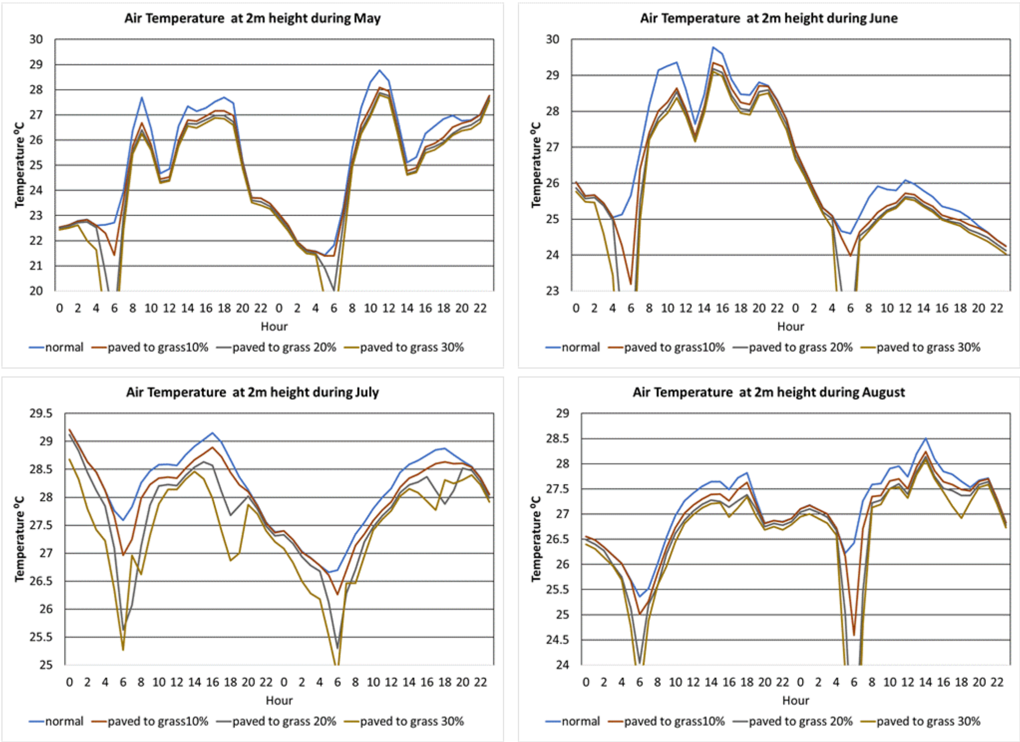

Figure 5.7 Air temperature for 2 days during May, June, July and August for the replacement of pavements with grass.

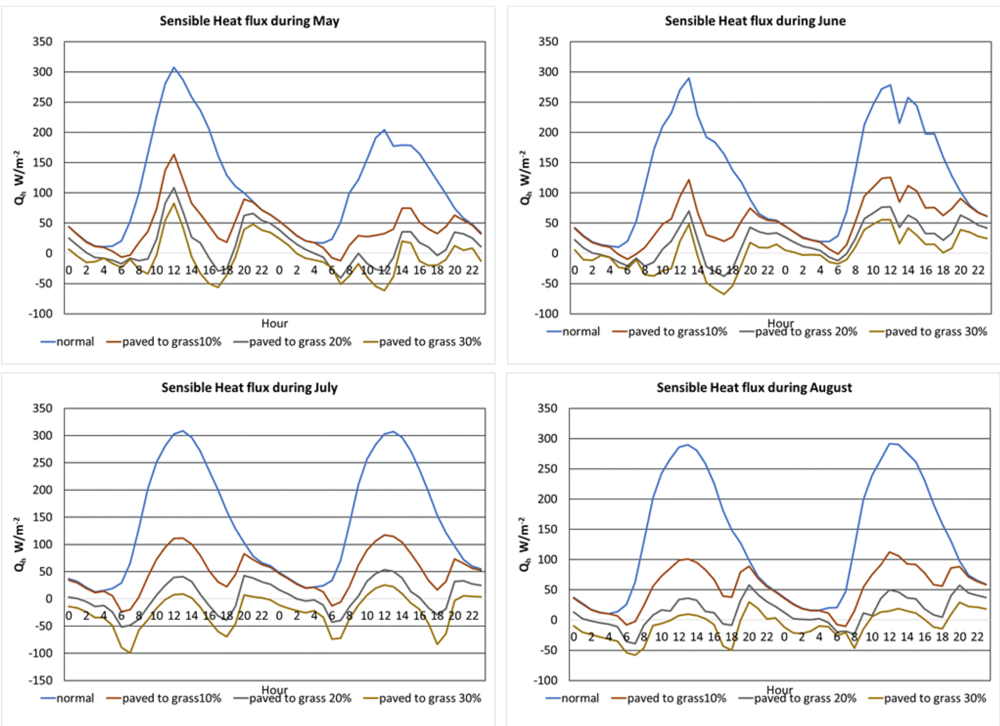

Figure 5.8 Sensible heat flux for 2 days during May, June, July and August for the replacement of pavements with grass.

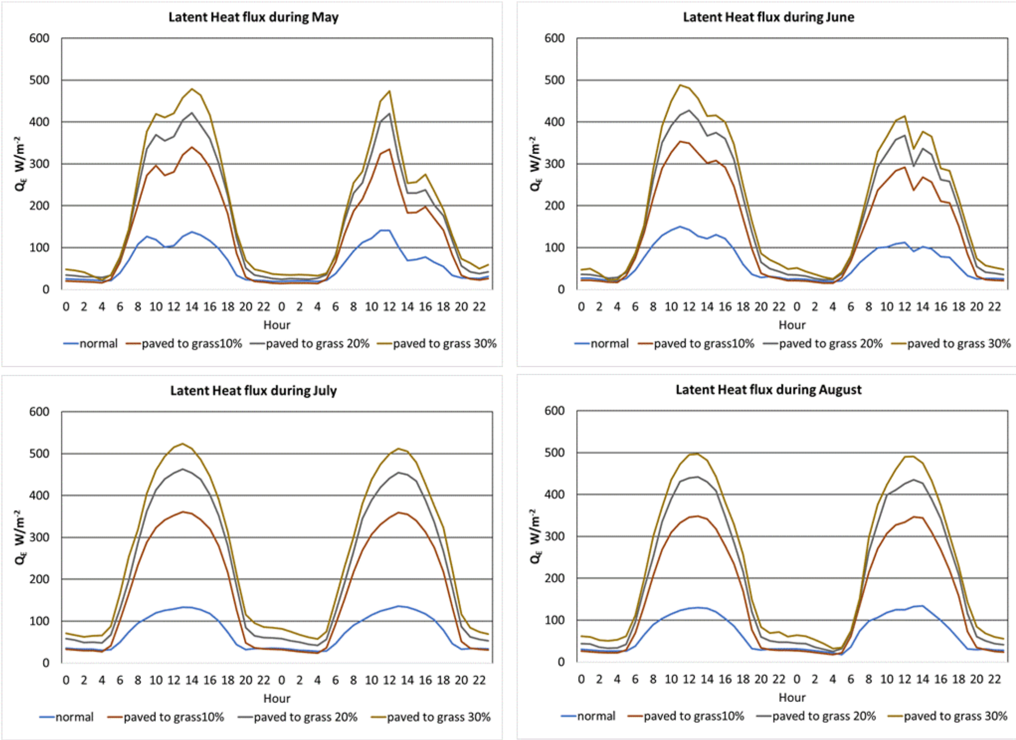

Figure 5.9 Latent heat flux for 2 days during May, June, July and August for the replacement of pavements with grass.

Table 5-3. Percentage of changes for all fluxes and for air temperature and relative humidity during daytime on monthly basis for the replacement of pavements with grass						
Month	Grass replace pavements 10%					
	Q*	ΔQs	QH	QE	Tair	RH
May	-0.92%	-4.76%	-41.44%	71.66%	-0.71%	3.73%
June	-0.94%	-4.81%	-54.75%	83.47%	-0.96%	6.65%
July	-3.55%	-17.53%	-45.38%	81.62%	-0.86%	5.47%
August	-1.09%	-2.34%	-43.99%	81.28%	-0.55%	3.02%
	Grass replace pavements 20%					
	Q*	ΔQs	QH	QE	Tair	RH
May	-1.84%	-9.27%	-157.34%	144.44%	-1.37%	7.82%
June	-1.88%	-9.25%	-109.00%	146.50%	-1.85%	15.88%
July	-7.09%	-34.30%	-79.21%	142.65%	-1.58%	12.78%
August	-2.31%	-4.52%	-83.04%	146.40%	-1.26%	9.61%
	Grass replace pavements 30%					
	Q*	ΔQs	QH	QE	Tair	RH
May	-2.76%	-13.51%	-313.03%	197.33%	-2.02%	12.27%
June	-2.82%	-13.32%	-144.70%	191.02%	-2.67%	22.63%
July	-10.63%	-50.26%	-103.44%	186.39%	-2.18%	17.32%
August	-3.53%	-6.53%	-111.86%	192.87%	-1.99%	16.80%

5.4 Replacement of pavements with trees and grass and roofs with grass

The specific scenario is a combination of two of the above and allows the study of the interrelations between the various NBS alternatives. The temperature decrease also occurs in this scenario and exceeds 1K during daytime as depicted in Figure 5.10. The percentage of change for the air temperature on monthly basis and during daytime is in all cases greater than 1% except May that shows a small increase. The decrease of Q^* is slightly higher than the one noticed when the roofs are replaced with grass due to the reduction of surface albedo for replacing higher percentage area of buildings and paved using higher albedo fractions (Table 6). The turbulent latent heat flux has the same behavior with the 1st scenario where the pavements are replaced with trees and grass and it is in accordance with the replacement of roofs with grass. The decrease of the Q_H in Figure 5.11 is explained by the increase of the turbulent latent heat flux in Figure 5.12. The results are similar with the scenarios 2 and 3, when grass replaces 30% of roof or pavements. This is attributed to the fact that trees are combined with grass replacing paved and roofs. A very small air temperature decrease occurs when trees and grass replace pavements and roofs respectively as depicted in Figure 5.10. The temperature difference exceeds 1K.

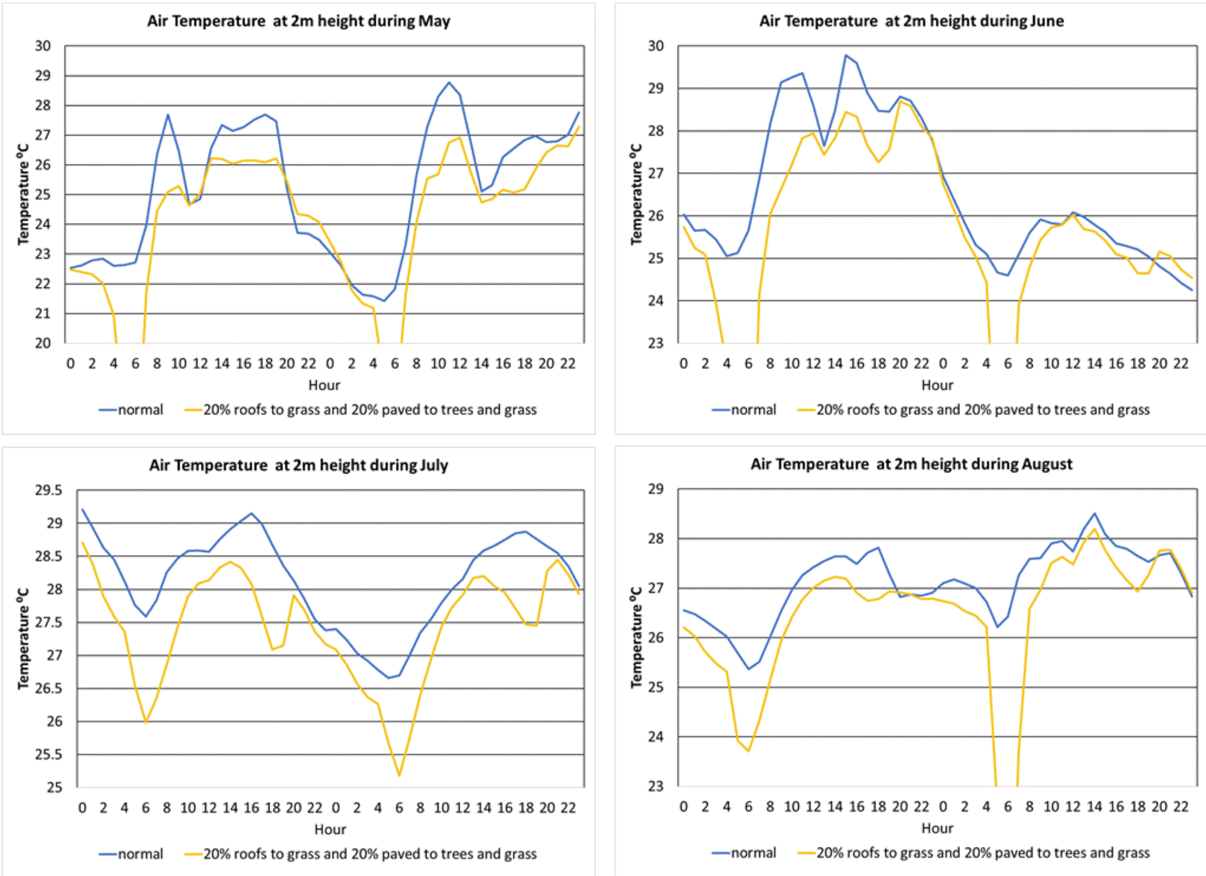

Figure 5.10. Air temperature for 2 days during May, June, July and August for the replacement of pavements with trees and grass and roofs with grass.

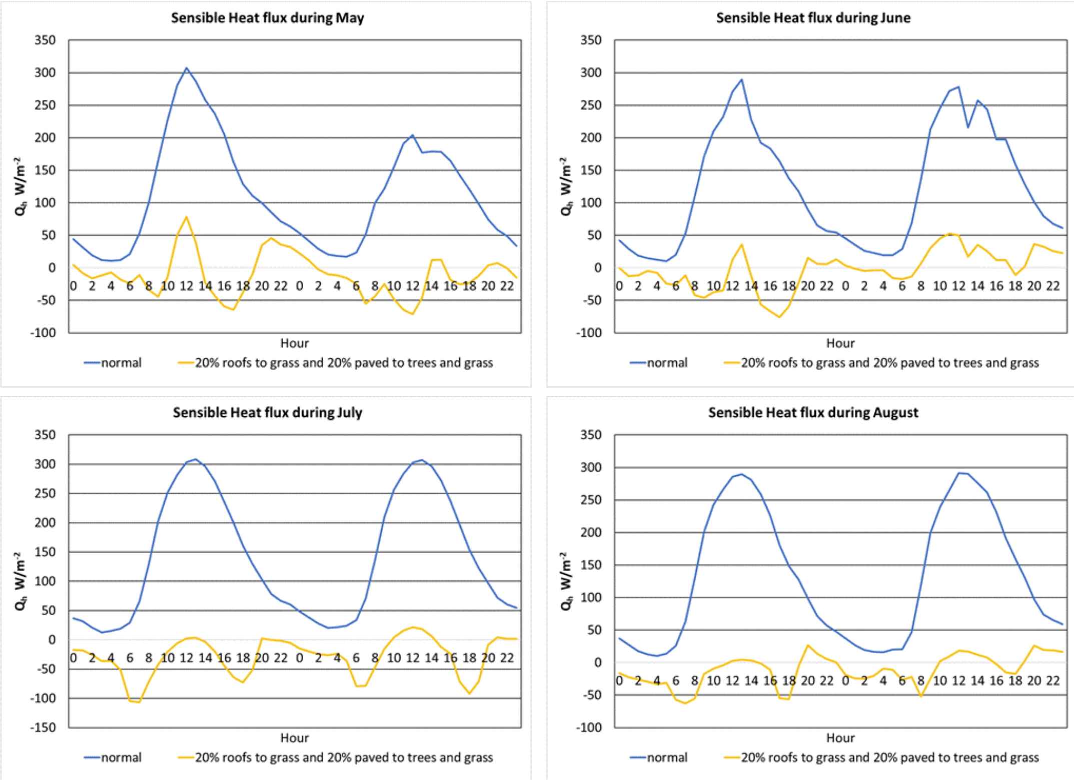

Figure 5.11 Sensible heat fluxes for 2 days during May, June, July and August for the replacement of pavements with trees and grass and roofs with grass

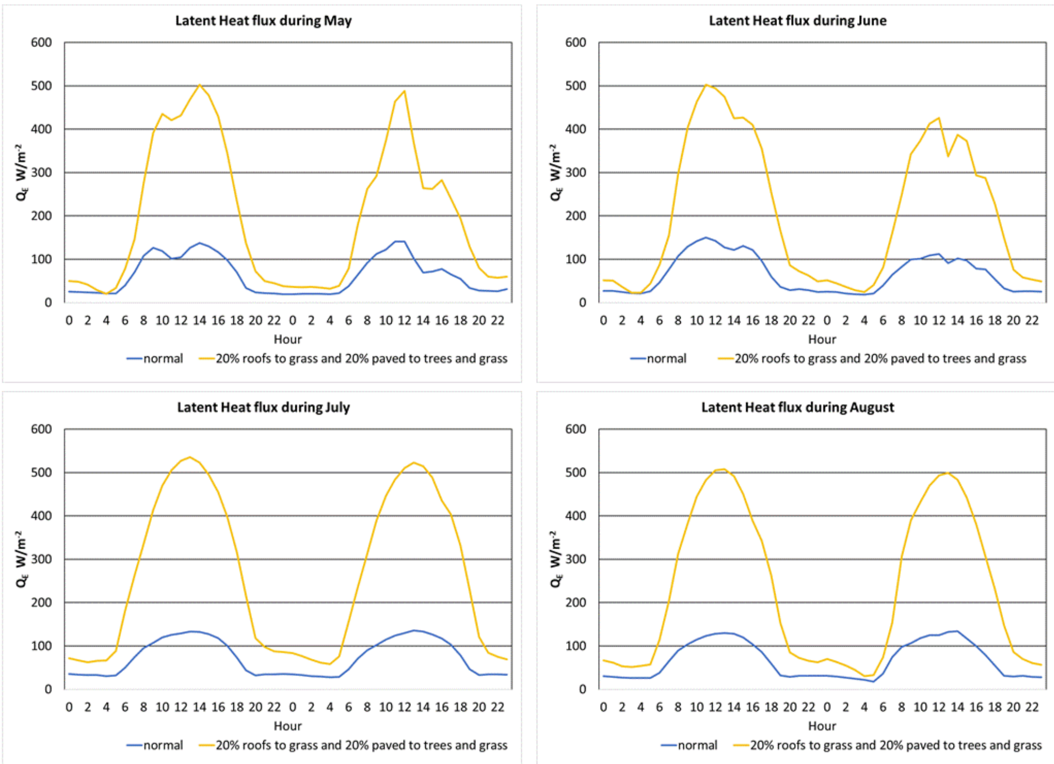

Figure 5.12 Latent heat fluxes for 2 days during May, June, July and August for the replacement of pavements with trees and grass and roofs with grass

Table 5-4. Percentage of changes for all fluxes and for air temperature and relative humidity during daytime on monthly basis for the replacement of pavements and roofs with trees and grass.

Month	Deciduous green trees replace pavements 10%					
	Q*	ΔQs	QH	QE	Tair	RH
May	-3.51%	-13.22%	-328.26%	206.59%	-1.07%	26.77%
June	-3.43%	-13.02%	-148.99%	197.64%	-2.84%	42.88%
July	-13.34%	-49.47%	-107.42%	192.83%	-2.17%	32.97%
August	-4.46%	-6.31%	-116.59%	199.59%	-2.11%	26.26%

5.5 Replacement of pavements with water

Although the scenario of replacing pavements with water bodies is very difficult to be applied in the specific site, the changes that occur are examined. The air temperature during two days is depicted in Figure 5.13, the sensible heat flux in Figure 5.14 and the turbulent latent heat flux in Figure 5.15, while the fluxes differences on monthly basis are tabulated in Table 7. A negligible air temperature decrease is noticed when water bodies are used during daytime. Also, during July, the differences are higher as depicted in Table 7. The Q^* is increased due to the decrease of water albedo versus the pavements. The same occurs for Q_E as expected and during daytime evaporation is increased, about 40 W/m^2 for May, also the RH is increased 1.09% due to Q_E increase. A decrease occurs for Q_H over 100 W/m^2, almost the same amount of Q_E increase, for all months based on the Eq. 12.

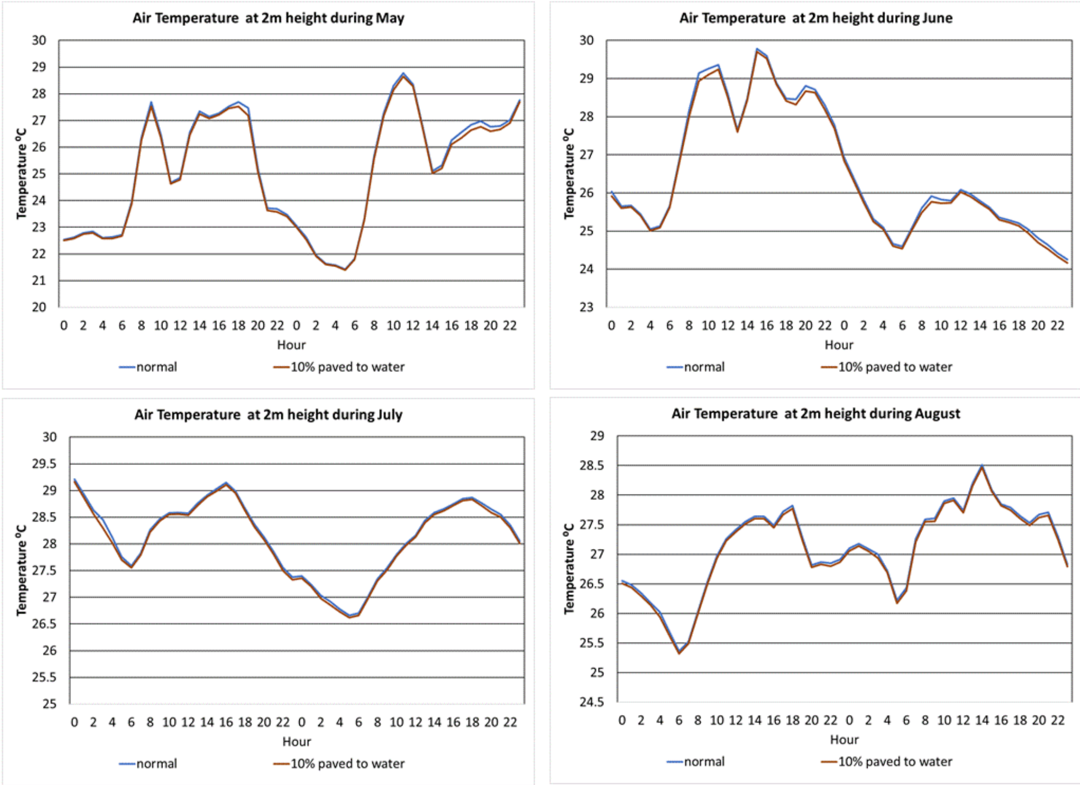

Figure 5.13 Air temperature for 2 days during May, June, July and August for the replacement of pavements with water

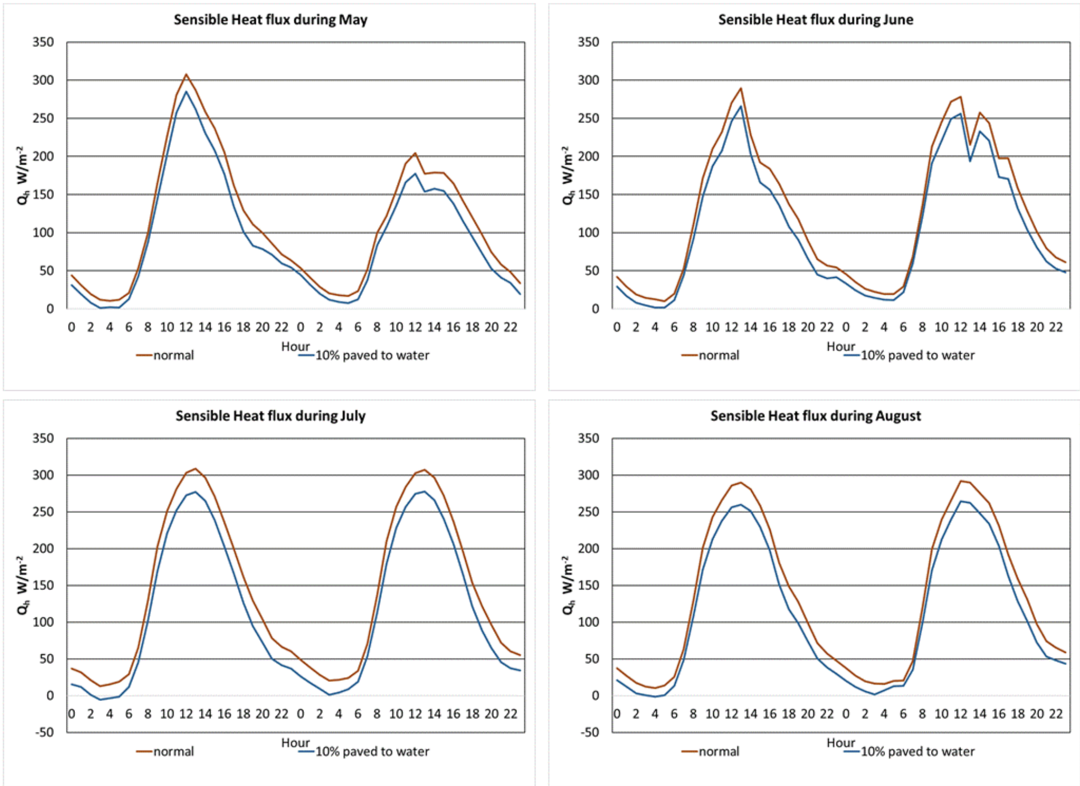

Figure 5.14 Sensible heat flux for 2 days during May, June, July and August for the replacement of pavements with water.

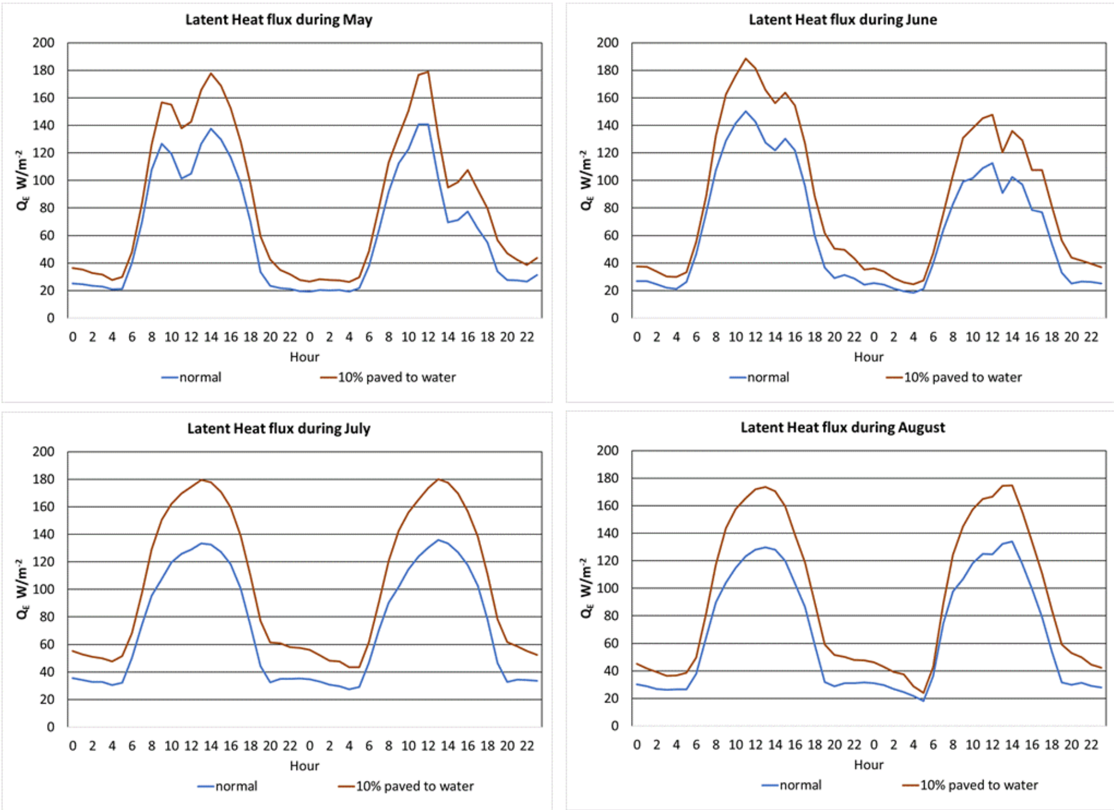

Figure 5.15 Turbulent Latent heat flux for 2 days during May, June, July and August for the replacement of pavements with water.

Table 5-5. Percentage of changes for all fluxes and for air temperature and relative humidity during the daytime on a monthly basis for the replacement of pavements with water						
Month	Green roofs replace existing roofs 10%					
	Q*	ΔQs	QH	QE	Tair	RH
May	0.00%	-1.41%	-82.89%	48.24%	-0.29%	0.96%
June	0.00%	-2.45%	-38.36%	40.26%	-0.25%	0.92%
July	0.00%	-4.62%	-21.33%	39.56%	-0.24%	1.09%
August	0.13%	-0.84%	-24.79%	42.45%	-0.17%	0.63%

The NBS scenarios simulation results using SUEWS model shows that albedo has a considerable impact on the net-all wave radiation as expected and seems to be a critical parameter when urban overheating mitigation measures are adopted. The application of NBS in the specific site shows that for all cases, i.e., green infrastructure or water bodies, the air temperature at 2m height is reduced versus the baseline. The percentage of replacement also plays a critical role in the improvement of climatic conditions at the site. Moreover, the lower the K↑ the higher the Q* and ΔQS are the energy that is trapped inside the built structures.

Since the version of the model we use does not allow to change the pavements' albedo, the interrelation of both highly reflective materials with NBS is not possible. Nevertheless, it should be noted that although with the replacement of pavements with grass, the albedo increases more that replacing roofs, the air temperature at 2 m is lower than the baseline and other cases. Therefore, incorporating highly reflective materials and green infrastructure will have a significant impact on reducing air temperature and surface temperature. An interesting finding is the impact of grass on the air temperature and relative humidity. The selection of the most appropriate solutions should consider the relative humidity of the air in the site to not create discomfort due to the increase of relative humidity. The grass seems to positively impact lowering air temperature without changing the relative humidity of the air significantly. Concerning water bodies, it is well recognized that they contribute to the decrease in air temperature, but relative humidity changes are considerable.

On the other hand, precipitation, irrigation, and water availability should be a significant concern in applying water bodies in cities. Using grass to replace roofs shows a reduction in the air temperature that reaches 2.67%, but also using grass to replace roofs can achieve a decrease of 2.22%. This reduction could be due to changes in the albedo that help reduce the energy balance. The rise of the turbulent latent heat flux that reaches almost 200% and the sensible heat flux reduction that reaches 100% shows that the amount of sensible heat flux is replaced by turbulent latent heat flux. This is also shown in the figures of sensible and turbulent latent heat flux (Figure 5.5,Figure 5.6,Figure 5.8,Figure 5.9,Figure 5.11,Figure 5.12)The turbulent latent heat flux from 120 W/m^2 in the baseline reaches 500 W/m^2 in some scenarios, and the sensible heat flux reduces to 100 W/m^2. The highest rise in turbulent latent heat flux is during August for combined roof and pavements to grass and trees that exceed 200%, and this is probably due to the significant change in the surface cover, i.e. the percentage of buildings and pavements is reduced from 95% to 55%. Using trees, there is a reduction about 0.79% to the temperature but not as high as when grass is used. This is probably due to the lower rise on albedo when the trees are applied, so the net radiation is higher than applying grass. The evapotranspiration increases more using grass and the turbulent latent heat flux also. As a result, the sensible heat flux is also (Figure 5.2) higher (100W/m^2) during the day instead of applying grass that, in every case, is lower than 100W/m^2 (Figure 5.5,Figure 5.8,Figure 5.11).

6.
CONCLUSION

The urban climate model SUEWS is evaluated and used for NBS cases to improve the microclimate inside the urban local environment. The site of interest is a dense urban area in the center of Heraklion, Greece, and consists of buildings and pavements mostly (≈93%). The model simulates the energy balance using meteorological data and incoming short-wave radiation.

The study shows that incorporating green infrastructure in various forms in a densely built city reduces the air temperature above ground while decreasing the sensible heat flux considerably. The air temperature and sensible heat flux are decreased according to the increase of the various spaces' green coverage. A significant finding is the change of relative humidity and turbulent latent heat flux, which seems very high in some cases especially when the grass is incorporated. This may significantly impact the urban comfort levels and be correlated with the local climatic conditions.

Although challenging to incorporate in urban outdoor spaces, water bodies have a considerable impact on the urban environment regarding outdoor temperature reduction and relative humidity. At the same time, they create pleasant spaces for citizens.

Therefore, the incorporation of NBS in cities change the energy balances significantly and modify the urban environment for the citizens' benefit. The quantification of the NBS impact on citizens' comfort and health is of great importance. At the same time, it contributes to reducing the energy demand for cooling and mitigation of the urban heat island.

7.
BIBLIOGRAPHY

1. UN Department of Economics and Social Affairs. World Population Prospects - Population Division - United Nations. The International Journal of Logistics Management. doi:10.1108/09574099810805708
2. Caprotti F, Cowley R, Datta A, et al. The New Urban Agenda: key opportunities and challenges for policy and practice. *Urban Res Pract*. 2017. doi:10.1080/17535069.2016.1275618
3. Ward HC, Kotthaus S, Järvi L, Grimmond CSB. Surface Urban Energy and Water Balance Scheme (SUEWS): Development and evaluation at two UK sites. *Urban Clim*. 2016;18:1-32. doi:10.1016/j.uclim.2016.05.001
4. Wilby RL. Constructing climate change scenarios of urban heat island intensity and air quality. *Environ Plan B Plan Des*. 2008;35(5):902-919. doi:10.1068/b33066t
5. Järvi L, Grimmond CSB, Christen A. The Surface Urban Energy and Water Balance Scheme (SUEWS): Evaluation in Los Angeles and Vancouver. *J Hydrol*. 2011;411(3-4):219-237. doi:10.1016/j.jhydrol.2011.10.001
6. Rafael S, Martins H, Sá E, Carvalho D, Borrego C, Lopes M. Influence of urban resilience measures in the magnitude and behaviour of energy fluxes in the city of Porto (Portugal) under a climate change scenario. *Sci Total Environ*. 2016;566-567:1500-1510. doi:10.1016/j.scitotenv.2016.06.037
7. Vargo J, Habeeb D, Stone B. The importance of land cover change across urban-rural typologies for climate modeling. *J Environ Manage*. 2013;114:243-252. doi:10.1016/j.jenvman.2012.10.007
8. Rafael S, Martins H, Marta-Almeida M, et al. Quantification and mapping of urban fluxes under climate change: Application of WRF-SUEWS model to Greater Porto area (Portugal). *Environ Res*. 2017;155(October 2016):321-334. doi:10.1016/j.envres.2017.02.033
9. Chrysoulakis, N. (Ed.), Castro, E. (Ed.), Moors E (Ed. . *Understanding Urban Metabolism: A Tool for Urban Planning*.; 2015. doi:https://doi.org/10.4324/9781315765846

10. Bonan GB. *Ecological Climatology: Concepts and Applications*. Cambridge University Press; 2002. https://books.google.gr/books?id=23TjswEACAAJ.

11. Martine G. Unleashing the potential of urban growth. In: *The State of the World Population 2007*. ; 2007. doi:ISBN 978-0-89714-807-8

12. Li D, Bou-Zeid E, Oppenheimer M. The effectiveness of cool and green roofs as urban heat island mitigation strategies. *Environ Res Lett*. 2014;9(5). doi:10.1088/1748-9326/9/5/055002

13. Kyriakodis G-E, Santamouris M. Using reflective pavements to mitigate urban heat island in warm climates - Results from a large scale urban mitigation project. *Urban Clim*. 2017. doi:10.1016/j.uclim.2017.02.002

14. Huynh Q, Craig W, Janssen I, Pickett W. Exposure to public natural space as a protective factor for emotional well-being among young people in Canada. *BMC Public Health*. 2013;13(1). doi:10.1186/1471-2458-13-407

15. Kolokotsa D, Lilli AA, Lilli MA, Nikolaidis NP. On the impact of nature-based solutions on citizens' health & well being. *Energy Build*. 2020;229. doi:10.1016/j.enbuild.2020.110527

16. Raymond CM, Frantzeskaki N, Kabisch N, et al. A framework for assessing and implementing the co-benefits of nature-based solutions in urban areas. *Environ Sci Policy*. 2017;77(July):15-24. doi:10.1016/j.envsci.2017.07.008

17. European Commission. Report from the Commission to the European Parliament and the Council - on the implementation of the EU Strategy on adaptation to climate change. *COM(2018) 738 Final*. 2018:19. https://eur-lex.europa.eu/legal-content/EN/TXT/?uri=COM:2018:738:FIN.

18. Somarakis G, Stagakis S, Chrysoulakis N. Thinknature Nature-Based Solutions Handbook. ThinkNature project funded by the EU Horizon 2020 research and innovation programme. 2019;(730338). doi:10.26225/ jerv-w202

19. Akbari H, Cartalis C, Kolokotsa D, et al. Local climate change and urban heat island mitigation techniques - The state of the art. *J Civ Eng Manag*. 2016;22(1). doi:10.3846/13923730.2015.1111934

20. Kolokotsa DD, Giannariakis G, Gobakis K, Giannarakis G, Synnefa A, Santamouris M. Cool roofs and cool pavements application in Acharnes, Greece. *Sustain Cities Soc*. 2018. doi:10.1016/j.scs.2017.11.035

21. Riahi K, Grübler A, Nakicenovic N. Scenarios of long-term socio-economic and environmental development under climate stabilization. *Technol Forecast Soc Change*. 2007. doi:10.1016/j.techfore.2006.05.026

22. Giorgetta MA, Jungclaus J, Reick CH, et al. Climate and carbon cycle changes from 1850 to 2100 in MPI-ESM simulations for the Coupled Model Intercomparison Project phase 5. *J Adv Model Earth Syst*. 2013. doi:10.1002/jame.20038

23. Augusto B, Roebeling P, Rafael S, Ferreira J, Ascenso A, Bodilis C. Short and medium- to long-term impacts of nature-based solutions on urban heat. *Sustain Cities Soc*. 2020. doi:10.1016/j.scs.2020.102122

24. Rafael S, Rodrigues V, Fernandes AP, Augusto B, Borrego C, Lopes M. Evaluation of urban surface parameterizations in WRF model using energy fluxes measurements in Portugal. *Urban Clim*. 2019. doi:10.1016/j.uclim.2019.100465

25. Kokkonen T V., Grimmond CSB, Räty O, et al. Sensitivity of Surface Urban Energy and Water Balance Scheme (SUEWS) to downscaling of reanalysis forcing data. *Urban Clim.* 2018. doi:10.1016/j.uclim.2017.05.001

26. Järvi L, Grimmond CSB, Taka M, Nordbo A, Setälä H, Strachan IB. Development of the Surface Urban Energy and Water Balance Scheme (SUEWS) for cold climate cities. *Geosci Model Dev*. 2014;7(4):1691-1711. doi:10.5194/gmd-7-1691-2014

27. Alexander PJ, Fealy R, Mills GM. Simulating the impact of urban development pathways on the local climate: A scenario-based analysis in the greater Dublin region, Ireland. *Landsc Urban Plan*. 2016. doi:10.1016/j.landurbplan.2016.02.006

28. Alexander PJ, Fealy R, Mills G. Spatial validation of an urban energy balance model using multi-temporal remotely sensed surface temperature. In: *2015 Joint Urban Remote Sensing Event, JURSE 2015*. ; 2015. doi:10.1109/JURSE.2015.7120500

29. Ao X, Grimmond CSB, Ward HC, et al. Evaluation of the Surface Urban Energy and Water Balance Scheme (SUEWS) at a dense urban site in Shanghai: Sensitivity to anthropogenic heat and irrigation. *J Hydrometeorol*. 2018. doi:10.1175/JHM-D-18-0057.1

30. Manoli G, Fatichi S, Schläpfer M, et al. Magnitude of urban heat islands largely explained by climate and population. *Nature*. 2019;573(7772):55-60. doi:10.1038/s41586-019-1512-9

31. Gobakis K, Kolokotsa D, Maravelaki-Kalaitzaki N, Perdikatsis V, Santamouris M. Development and analysis of advanced inorganic coatings for buildings and urban structures. *Energy Build*. 2015;89. doi:10.1016/j.enbuild.2014.10.081

32. Kolokotsa D, Diakaki C, Papantoniou S, Vlissidis A. Numerical and experimental analysis of cool roofs application on a laboratory building in Iraklion, Crete, Greece. *Energy Build*. 2012;55. doi:10.1016/j.enbuild.2011.09.011

33. Järvi L, Grimmond CSB, Taka M, Nordbo A, Setälä H, Strachan IB. Development of the Surface Urban Energy and Water Balance Scheme (SUEWS) for cold climate cities. *Geosci Model Dev*. 2014. doi:10.5194/gmd-7-1691-2014

34. Borrego C, Monteiro A, Martins H, et al. Air quality plan for ozone: an urgent need for North Portugal. *Air Qual Atmos Heal*. 2016. doi:10.1007/s11869-015-0352-5

35. Monteiro A, Ferreira J, Ribeiro I, et al. Air quality over portugal in 2020. *Atmos Pollut Res*. 2015. doi:10.5094/APR.2015.087

36. Rafael S, Martins H, Sá E, Carvalho D, Borrego C, Lopes M. Influence of urban resilience measures in the magnitude and behaviour of energy fluxes in the city of Porto (Portugal) under a climate change scenario. *Sci Total Environ*. 2016. doi:10.1016/j.scitotenv.2016.06.037

37. Oke TR. *Boundary Layer Climates, Second Edition*.; 1987. doi:10.1017/CBO9781107415324.004

38. Grimmond CSB, Oke TR, Steyn DG. Urban Water Balance: 1. A Model for Daily Totals. *Water Resour Res*. 1986;22(10):1397-1403. doi:10.1029/WR022i010p01397

39. Grimmond CSB, Oke TR. An evapotranspiration-interception model for urban areas. *Water Resour Res*. 1991;27(7):1739-1755. doi:10.1029/91WR00557

40. Grimmond CSB, Cleugh HA, Oke TR. An objective urban heat storage model and its comparison with other schemes. *Atmos Environ Part B, Urban Atmos*. 1991;25(3):311-326. doi:10.1016/0957-1272(91)90003-W

41. Offerle B, Grimmond CSB, Oke TR. Parameterization of net all-wave radiation for urban areas. *J Appl Meteorol*. 2003;42(8):1157-1173. doi:10.1175/1520-0450(2003)042<1157:PONARF>2.0.CO;2

42. Grimmond CSB, Oke TR. Turbulent heat fluxes in urban areas: Observations and a local-scale urban meteorological parameterization scheme (LUMPS). *J Appl Meteorol*. 2002;41(7):792-810. doi:10.1175/1520-0450(2002)041<0792:THFIUA>2.0.CO;2

43. Lindberg F, Grimmond S, Onomura S, Järvi LJ. Urban Multi-scale Environmental Predictor . *An Integr tool urban Climatol Clim sensitive Plan Appl* . 2015. http://www.meteo.fr/icuc9/presentations.html.

44. Karsisto P, Fortelius C, Demuzere M, et al. Seasonal surface urban energy balance and wintertime stability simulated using three land-surface models in the high-latitude city Helsinki. *Q J R Meteorol Soc*. 2016;142(694):401-417. doi:10.1002/qj.2659

45. Alexander PJ, Mills G, Fealy R. Using LCZ data to run an urban energy balance model. *Urban Clim*. 2015;13:14-37. doi:10.1016/j.uclim.2015.05.001

46. Loridan T, Grimmond CSB. Characterization of energy flux partitioning in urban environments: Links with surface seasonal properties. *J Appl Meteorol Climatol*. 2012;51(2):219-241. doi:10.1175/JAMC-D-11-038.1

47. Crawford TM, Duchon CE. An improved parameterization for estimating effective atmospheric emissivity for use in calculating daytime downwelling longwave radiation. *J Appl Meteorol*. 1999;38(4):474-480. doi:10.1175/1520-0450(1999)038<0474:AIPFEE>2.0.CO;2

48. Chrysoulakis N, Grimmond CSB. Understanding and reducing the anthropogenic heat emission. *Urban Clim Mitig Tech*. 2016:27-40. doi:10.4324/9781315765839

49. Sailor DJ, Georgescu M, Milne JM, Hart MA. Development of a national anthropogenic heating database with an extrapolation for international cities. *Atmos Environ*. 2015. doi:10.1016/j.atmosenv.2015.07.016

50. Kłysik K. Spatial and seasonal distribution of anthropogenic heat emissions in Lodz, Poland. *Atmos Environ*. 1996. doi:10.1016/1352-2310(96)00043-X

51. Taha H. Urban climates and heat islands: Albedo, evapotranspiration, and anthropogenic heat. *Energy Build*. 1997. doi:10.1016/s0378-7788(96)00999-1

52. Hamilton IG, Davies M, Steadman P, Stone A, Ridley I, Evans S. The significance of the anthropogenic heat emissions of London's buildings: A comparison against captured shortwave solar radiation. *Build Environ*. 2009. doi:10.1016/j.buildenv.2008.05.024

53. Ichinose T, Shimodozono K, Hanaki K. Impact of anthropogenic heat on urban climate in Tokyo. In: *Atmospheric Environment*. ; 1999. doi:10.1016/S1352-2310(99)00132-6

54. Sailor DJ, Vasireddy C. Correcting aggregate energy consumption data to account for variability in local weather. *Environ Model Softw*. 2006. doi:10.1016/j.envsoft.2005.08.001

55. Ward HC, Evans JG, Grimmond CSB. Multi-season eddy covariance observations of energy, water and carbon fluxes over a suburban area in Swindon, UK. *Atmos Chem Phys*. 2013;13(9):4645-4666. doi:10.5194/acp-13-4645-2013

56. Doll D, Ching JKS, Kaneshiro J. Parameterization of subsurface heating for soil and concrete using net radiation data. *Boundary-Layer Meteorol*. 1985. doi:10.1007/BF00122000

57. McCaughey JH. Energy balance storage terms in a mature mixed forest at Petawawa, Ontario - A case study. *Boundary-Layer Meteorol*. 1985;31(1):89-101. doi:10.1007/BF00120036

58. Yoshida A, Tominaga K, Watatani S. Field measurements on energy balance of an urban canyon in the summer season. *Energy Build*. 1990;15(3-4):417-423. doi:10.1016/0378-7788(90)90016-C

59. Arnfield AJ, Grimmond CSB. An urban canyon energy budget model and its application to urban storage heat flux modeling. *Energy Build*. 1998. doi:10.1016/s0378-7788(97)00026-1

60. Meyn SK, Oke TR. Heat fluxes through roofs and their relevance to estimates of urban heat storage. *Energy Build*. 2009;41(7):745-752. doi:10.1016/j.enbuild.2009.02.005

61. Sun T, Wang ZH, Ni GH. Revisiting the hysteresis effect in surface energy budgets. *Geophys Res Lett*. 2013;40(9):1741-1747. doi:10.1002/grl.50385

62. Grimmond CSB, Oke TR. Heat storage in urban areas: Local-scale observations and evaluation of a simple model. *J Appl Meteorol*. 1999. doi:10.1175/1520-0450(1999)038<0922:HSIUAL>2.0.CO;2

63. Roberts SM, Oke TR, Grimmond CSB, Voogt JA. Comparison of four methods to estimate urban heat storage. *J Appl Meteorol Climatol*. 2006;45(12):1766-1781. doi:10.1175/JAM2432.1

64. Krinner G, Viovy N, de Noblet-Ducoudré N, et al. A dynamic global vegetation model for studies of the coupled atmosphere-biosphere system. *Global Biogeochem Cycles*. 2005. doi:10.1029/2003GB002199

65. Best MJ, Pryor M, Clark DB, et al. The Joint UK Land Environment Simulator (JULES), model description – Part 1: Energy and water fluxes. *Geosci Model Dev*. 2011. doi:10.5194/gmd-4-677-2011

66. De Kauwe MG, Kala J, Lin YS, et al. A test of an optimal stomatal conductance scheme within the CABLE land surface model. *Geosci Model Dev*. 2015. doi:10.5194/gmd-8-431-2015

67. Jarvis PG. The interpretation of the variations in leaf water potential and stomatal conductance found in canopies in the field. *Philos Trans R Soc London B, Biol Sci*. 1976;273(927):593-610. doi:10.1098/rstb.1976.0035

68. Ogink-Hendriks MJ. Modelling surface conductance and transpiration of an oak forest in The Netherlands. *Agric For Meteorol*. 1995. doi:10.1016/0168-1923(94)02180-R

69. Chrysoulakis N, Grimmond S, Feigenwinter C, et al. Urban energy exchanges monitoring from space. *Sci Rep*. 2018. doi:10.1038/s41598-018-29873-x

70. Christen A. The IAUC Urban Flux Network An international network of micrometeorological flux towers. 2009;(December).

71. Stagakis S, Chrysoulakis N, Spyridakis N, Feigenwinter C, Vogt R. Eddy Covariance measurements and source partitioning of CO2 emissions in an urban environment: Application for Heraklion, Greece. *Atmos Environ*. 2019;201(November 2018):278-292. doi:10.1016/j.atmosenv.2019.01.009

72. Marconcini M, Heldens W, Del Frate F, Latini D, Mitraka Z, Lindberg F. EO-based products in support of urban heat fluxes estimation. *2017 Jt Urban Remote Sens Event, JURSE 2017*. 2017:0-3. doi:10.1109/JURSE.2017.7924592

73. Lindberg F, Grimmond CSB, Gabey A, et al. Urban Multi-scale Environmental Predictor (UMEP): An integrated tool for city-based climate services. *Environ Model Softw*. 2018;99:70-87. doi:10.1016/j.envsoft.2017.09.020

74. Sun T, Järvi L, Omidvar H, et al. Urban-Meteorology-Reading/SUEWS: 2019a Release. November 2019. doi:10.5281/ZENODO.3533450

75. Zimmermann NE, Washington-Allen RA, Ramsey RD, et al. Modern Remote Sensing for Environmental Monitoring of Landscape States and Trajectories. In: ; 2007. doi:10.1007/978-1-4020-4436-6_6

76. Grimmond CSB, Oke TR. Aerodynamic properties of urban areas derived from analysis of surface form. *J Appl Meteorol*. 1999. doi:10.1175/1520-0450(1999)038<1262:APOUAD>2.0.CO;2

77. Stagakis S, Burud I, Thiis T, et al. Spatiotemporal monitoring of surface temperature in an urban area using UAV imaging and tower-mounted radiometer measurements. *2019 Jt Urban Remote Sens Event, JURSE 2019*. 2019;(May). doi:10.1109/JURSE.2019.8808958

78. Kotthaus S, Grimmond CSB. Energy exchange in a dense urban environment - Part II: Impact of spatial heterogeneity of the surface. *Urban Clim*. 2014;10(P2):281-307. doi:10.1016/j.uclim.2013.10.001